

Banner appropriate to article type will appear here in typeset article

Resolvent-Based Optimisation for Invariant Flows

Thomas Burton^{1†}, Sean Symon¹ and Davide Lasagna¹

¹University of Southampton, Faculty of Engineering and Physical Sciences, University Road, Southampton SO17 1BJ, UK

(Received xx; revised xx; accepted xx)

We present a robust optimisation framework for computing invariant solutions of wall-bounded flows by recasting the Navier–Stokes equations as a variational problem as established in Ashtari & Schneider, *JFM* (2023). The approach minimises the residual of the governing equations over a finite time horizon, seeking periodic or equilibrium solutions. A novel contribution is made by including a Galerkin projection onto a basis of divergence-free modes that satisfy the no-slip boundary conditions. This projection not only makes the variational framework applicable to wall-bounded flows but it also yields a low-order representation of the dynamics. The basis is derived from resolvent analysis, which provides an orthonormal set. We demonstrate the method on a 2D3C formulation of rotating plane Couette flow, obtaining exact equilibrium and periodic solutions consistent with direct numerical simulations. The conditioning of the optimisation problem is analysed in detail, showing that convergence rates depend on the stability properties of the targeted solutions. Finally, we highlight a direct link between the conditioning of the optimisation and the structure of the resolvent operator, suggesting a unifying perspective on both the efficiency of the optimisation and the dynamical significance of resolvent modes.

Key words:

1. Introduction

Turbulence is often treated as a stochastic process. Progress in its study has largely come from statistical descriptions that exploit the self-similarity across different scales, yielding a universal picture of small-scale dynamics. Such approaches, however, offer little insight into the geometry-dependent large-scale structures or the physical mechanisms that govern turbulence more generally. An alternative view of turbulence, motivated by the theory of chaos for low-dimensional dissipative systems, was proposed by Eberhard Hopf (Hopf 1942, 1948). In this view, the state of a fluid is asymptotically confined to a finite-dimensional invariant subspace embedded within the infinite-dimensional state-space of the flow. The dimension of this invariant subspace can be much smaller than the infinite-dimensional nature of the state would suggest, owing to the strong dissipative power of viscosity. As the Reynolds number increases the dimension of the invariant subspace usually increases allowing for

† Email address for correspondence: T.P.Burton@soton.ac.uk

more complex temporal evolution of the flow and requiring more degrees of freedom to accurately describe the resulting smaller scale motions observed. However, understanding this invariant subspace is quite difficult as a result of its complex fractal structure indicative of strange attractors (Ruelle & Takens 1971; Aizawa 1982).

For low-dimensional chaotic systems, the complex structure of strange attractors has been shown in Auerbach *et al.* (1987) to be determined by the set of Unstable Periodic Orbits (UPOs) embedded within the attractor, providing a “skeleton” for the dynamics. It was shown in Cvitanović (1988) and Cvitanović (1995) that building these UPOs up in the form of a weighted sum can yield the ergodic properties of the dynamics on the strange attractor (Artuso *et al.* 1990). This method is called cycle expansion theory. Analogously, exact nonlinear solutions to the Navier-Stokes equations have been numerically shown to exist, dubbed Exact Coherent Structures (ECSs) due to their close resemblance to coherent structures observed in experiment and Direct Numerical Simulation (DNS) studies. The exact nature of these ECSs are not yet fully understood, however, there is evidence that turbulent flows repeatedly shadow ECSs for a finite amount of time before moving away along one of the unstable manifolds of the solution towards a different ECSs (Suri *et al.* 2020; Krygier *et al.* 2021; Crowley *et al.* 2022). It was also demonstrated (Yalnız *et al.* 2021; Page *et al.* 2024) that using ECSs in a cycle expansion approach yields accurate statistics of the turbulent flow. The results do however generally rely on a tuning of the relative contribution of each ECS as opposed to deriving them exactly according cycle expansion theory (Wang *et al.* 2025). The numerical computation of ECSs was first shown in Nagata (1990) and Nagata (1997) where equilibrium and travelling wave solutions to the plane-Couette flow were computed. Since then there has been regular work to expand the sets of solutions for various flows (Waleffe 1998, 2001; Faisst & Eckhardt 2003; Wedin & Kerswell 2004; Viswanath 2007; Pringle & Kerswell 2007; Gibson *et al.* 2008; Waleffe 2009; Itano & Generalis 2009; Wedin *et al.* 2009; Okino *et al.* 2010; Uhlmann *et al.* 2010; Willis *et al.* 2013; Nagata *et al.* 2021). A general review of the relevance of invariant solutions to fluid turbulence can be found in Kawahara *et al.* (2012).

The numerical methods employed to find ECSs are generally divided into local and global approaches. Local methods, primarily shooting algorithms, are initialised with a flow snapshot that is evolved forward over the current period, with the mismatch between initial and final states used to update both the initial condition and the period. Examples include Christiansen *et al.* (1997), Tomoaki & Sadayoshi (2001), Kawahara & Kida (2001), Sánchez *et al.* (2004), van Veen *et al.* (2006), Cvitanović & Gibson (2010), and Chandler & Kerswell (2013). Shooting algorithms are typically combined with a Newton–Krylov iteration, where the Jacobian system is solved by GMRES (Saad & Schultz 1986) to avoid explicit formation and prohibitive memory costs. However, this approach is highly sensitive to initial conditions due to the chaotic nature of the dynamics, requiring initialisation from close recurrences. Convergence becomes increasingly difficult for longer periods. To address this, multiple-shooting methods (Christiansen *et al.* 1997) replace the single trajectory with shorter segments matched simultaneously, improving conditioning and enabling parallel computation (Sánchez *et al.* 2004). Further robustness is achieved by adding a hookstep to the Newton–GMRES iteration (Dennis & Schnabel 1983; Viswanath 2007, 2009), which, when combined with multiple-shooting methods, represents the most effective way of computing invariant solutions in fluid flows. Nevertheless, challenges remain as the system size grows (Veen *et al.* 2019).

Global methods instead act on a full spatio-temporal field that already satisfies the required invariance, iteratively modifying it until the governing equations are solved to a prescribed tolerance. The Newton flow method introduced by Lan & Cvitanović (2004) formulates the problem through variational dynamics that converge exponentially to invariant solutions,

with an over-relaxation factor mitigating the erratic behaviour of standard Newton iterations. Unlike shooting methods, these global approaches avoid exponential trajectory divergence and are generally more robust. However, the Newton flow method is not naturally matrix-free, as each iteration requires forming and solving an $N \times N$ Jacobian system, with N the degrees of freedom. This makes the approach prohibitively costly for high-dimensional systems (Fazendeiro *et al.* 2010). Practical implementations must therefore employ GMRES, as in local methods. Despite these advantages, the method still suffers from sensitivity to initial guesses owing to the limited convergence radius of Newton iterations.

An alternative global approach is to recast the search for invariant solutions as an optimisation problem rather than root finding. Here, the objective functional measures the total violation of the governing equations over the spatio-temporal domain. Introduced by Farazmand (2016) for equilibrium and travelling-wave solutions in 2D Kolmogorov flow, this method is formulated as the adjoint of the Newton descent of Lan & Cvitanović (2004). Crucially, it is naturally matrix-free and therefore well-suited to high-dimensional systems. The variational optimisation approach demonstrated markedly greater robustness to initial conditions, enabling convergence from a wider set of guesses and uncovering previously unknown solutions. More recently, Azimi *et al.* (2022), and Ashtari & Schneider (2023) extended the framework separately to periodic flows and to cases with no-slip boundary conditions, respectively. In the latter study, the Influence Matrix (IM) method (Kleiser & Schumann 1980) was employed to enforce no-slip constraints consistently with the Pressure Poisson Equation (PPE), thereby avoiding boundary errors that arise when the PPE is solved without an explicit pressure condition.

Despite its advantages, the variational optimisation method still faces challenges. While the IM method provides a clear strategy for equilibria in wall-bounded domains, its extension to temporally periodic fields is unclear, leaving open the problem of a general approach for periodic solutions in such settings. Moreover, the improved robustness compared with Newton-based methods comes at the cost of losing quadratic convergence. Convergence is initially rapid but slows considerably near the minimum, largely due to the use of gradient descent, which is notoriously inefficient in this regime (Nocedal & Wright 2006). Algorithms incorporating curvature information could improve performance. Farazmand (2016) addressed this by adopting a hybrid strategy, initially using optimisation to approach the solution after which Newton–GMRES–hookstep is employed to accelerate convergence. More recently, Ashtari & Schneider (2023) improved efficiency of variational optimisation by employing an extrapolation technique with Dynamic Mode Decomposition (DMD). Nevertheless, the method remains hampered by a significantly slower convergence rate than Newton-based method, particularly as problem dimension increases. Hence, it is desirable to develop modifications that improve convergence without switching methods, while retaining compatibility with complex no-slip geometries.

In this work, the variational optimisation framework is extended with a Galerkin projection, making it directly applicable to wall-bounded flows with no-slip boundaries. This projection enforces incompressibility and no-slip constraints while decoupling pressure and velocity. The basis is constructed from resolvent modes, which form a divergence-free, orthonormal set satisfying the boundary conditions. Our approach is similar to Li & Lasagna (2025), who used a projection-based optimisation for lid-driven cavity flow. In this work, however, resolvent modes replace SPOD modes, removing the need for fully resolved flow data and enabling the construction of exact solutions rather than reduced-order models. Resolvent analysis, a widely used tool for stability, control, and modelling (Gayme 2010; Garnaudo *et al.* 2013; Gómez *et al.* 2016; Beneddine *et al.* 2017; Symon *et al.* 2018; Gayme & Minnick 2019; Jin *et al.* 2022), has been shown to provide dynamically significant bases for unstable solutions (Sharma *et al.* 2016) and to enable new invariant solutions via “projection-then-search” (Ahmed &

Sharma 2020). It has also been applied to reduced-order modelling, e.g. Taylor vortex flow in Barthel *et al.* (2021). Our work builds on these ideas by employing resolvent modes within a variational framework, where the Galerkin projection both enforces boundary constraints and yields a reduced-order model tailored to optimisation. Here, truncation is used not only to approximate turbulence, as in Barthel *et al.* (2021), but to enable computation of exact invariant solutions and accelerate convergence. To further address the slow convergence of variational optimisation, we depart from gradient-descent schemes (Farazmand 2016; Azimi *et al.* 2022; Ashtari & Schneider 2023) and instead use quasi-Newton algorithms such as L-BFGS and conjugate gradient, which achieve substantially faster convergence.

The remainder of the paper is organised as follows. Section 2 introduces the variational optimisation methodology and the Galerkin projection used to enforce incompressibility and no-slip boundary conditions. Section 3 presents the derivation of the resolvent modes forming the projection basis. Section 4 introduces the 2D3C formulation of Rotating Plane Couette Flow (RPCF) and features a basic analysis of the behaviour of the flow at various Reynolds number regimes. Section 5 then demonstrates the projected variational optimisation methodology using resolvent analysis, featuring equilibrium and periodic solutions. The underlying mechanics governing the conditioning of the optimisation is then discussed in section 6, providing a novel link between resolvent analysis and the convergence rate. Finally, section 7 concludes with a discussion of the main results of this work and the possible avenues for future work.

2. Methodology

In section 2.1, the variational optimisation methodology for wall-bounded flows is described. The methodology is applicable to general wall-bounded flows, however here it is specialised for flows with a single inhomogeneous direction. This is to be more in line with the derivation in Ashtari & Schneider (2023). In section 2.2 the Galerkin projection is introduced as a way to solve to issues that arise due to the presence of no-slip boundary conditions. A more verbose derivation and discussion of the implications can be found in Burton (2025).

2.1. Variational Optimisation for Wall-Bounded Periodic Flows

Consider the non-dimensional Navier-Stokes equations and continuity equation

$$\frac{\partial \mathbf{u}}{\partial t} = -\nabla p - (\mathbf{u} \cdot \nabla) \mathbf{u} + \frac{1}{Re} \Delta \mathbf{u}, \quad (2.1a)$$

$$\nabla \cdot \mathbf{u} = 0, \quad (2.1b)$$

where Re denotes the Reynolds number. The exact definition is delays until section 4 where the particular flow studied in detail in this work is defined. The velocity \mathbf{u} is an 3-dimensional vector field defined over a compact 3-dimensional space, denoted as $\Omega = [0, L_x] \times [-1, 1] \times [0, L_z]$ with a boundary denoted as $\partial\Omega$. p denotes the scalar pressure field defined on the same space as \mathbf{u} . The coordinates for Ω are the single inhomogeneous wall-normal direction (y) normalised with respect to the channel height, and the streamwise and spanwise directions (x and z respectively) which are statistically homogeneous. Using these Cartesian coordinates the Laplace operator is defined as $\Delta = \partial^2/\partial x^2 + \partial^2/\partial y^2 + \partial^2/\partial z^2$. Homogeneity of the flow is modelled with periodic boundary conditions in the streamwise and spanwise directions, while the no-slip boundary conditions are imposed at the wall

$$\mathbf{u}|_{y=\pm 1} = \mathbf{u}_w, \quad (2.2)$$

where \mathbf{u}_w is velocity of the wall. The velocity field \mathbf{u} is also defined over a finite time horizon fixed by the orbit period T , thus $t \in [0, T)$. The combination of the spacial and temporal

domains is defined as $\Omega_t = \Omega \times [0, T)$. The inner-product on this space is defined as

$$\langle \mathbf{u}, \mathbf{v} \rangle_{\Omega_t} = \int_0^T \int_0^{L_z} \int_{-1}^1 \int_0^{L_x} \mathbf{u}^\top \cdot \mathbf{v} \, dx \, dy \, dz \, dt, \quad (2.3)$$

where $(\cdot)^\top$ denotes the transpose. This inner-product induces an associated norm $\|\mathbf{u}\|_{\Omega_t} = \sqrt{\langle \mathbf{u}, \mathbf{u} \rangle_{\Omega_t}}$. Thus, any velocity fields that has a finite norm under this definition is an element of the underlying Hilbert space, denoted with χ , and has finite kinetic energy. We now define the space of all periodic incompressible flow fields that obey the boundary and periodicity conditions

$$\mathcal{P}_T = \{ \mathbf{u} \in \chi : \nabla \cdot \mathbf{u} = 0, \mathbf{u}|_{t=0} = \mathbf{u}|_{t=T}, \mathbf{u}|_{y=\pm 1} = \mathbf{u}_w, \mathbf{u} \text{ obeys periodic BCs} \}. \quad (2.4)$$

The elements of \mathcal{P}_T are state-space loops that do not necessarily obey (2.1a). In general T is not known a priori and should be included as part of the optimisation problem. The goal is to derive a method that converges to the subset of \mathcal{P}_T that obey (2.1a). This can be done by introducing a mapping $\mathcal{R}: \mathcal{P}_T \rightarrow \mathbb{R}_{\geq 0}$ such that $\mathcal{R}[\mathbf{u}] = 0$ if and only if $\mathbf{u} \in \mathcal{P}_T$ and \mathbf{u} satisfies (2.1a), otherwise $\mathcal{R} > 0$. This is equivalent to defining an objective function whose global minima ($\mathcal{R} = 0$) correspond to periodic solutions of (2.1a) that are divergence-free and obey the no-slip and periodicity boundary conditions, called here the global residual. To obtain the global residual, first a local residual that quantifies the violation of the Navier-Stokes equations at every point in Ω_t needs to be defined as follows

$$\mathbf{r} = \frac{\partial \mathbf{u}}{\partial t} + \nabla p + (\mathbf{u} \cdot \nabla \mathbf{u}) - \frac{1}{Re} \Delta \mathbf{u}. \quad (2.5)$$

Figure 1 shows a representation of the local residual defined on all points of a state-space loop representing a periodic flow. The local residual spans the distance between the rate of change of a state-space loop and the forcing imposed by the Navier-Stokes equations. The task of finding periodic solutions to (2.1a) in the space \mathcal{P}_T can now be stated in terms of the following optimisation problem

$$\min_{\mathbf{u} \in \mathcal{P}_T, T} \mathcal{R}[\mathbf{u}] = \frac{1}{2} \|\mathbf{r}\|_{\Omega_t}^2. \quad (2.6)$$

where the functional $\mathcal{R}[\mathbf{u}]$ is called the global residual. Geometrically, minimising \mathcal{R} is equivalent to continuously deforming a loop in the state-space of the flow field, constrained to the linear subspace that define the boundary conditions and incompressibility conditions. This process terminates when the rate of change of the state vector and the right-hand side of (2.1a) are as closely aligned as possible.

To be able to solve this optimisation problem in practice, the gradient of \mathcal{R} with respect to the field \mathbf{u} is required, referred to as the functional derivative and denoted as $\delta \mathcal{R} / \delta \mathbf{u}$. This expression can be obtained by adding a perturbation to the velocity field denoted as \mathbf{v} such that $\mathbf{u} \rightarrow \mathbf{u} + \epsilon \mathbf{v}$ where $\epsilon \in \mathbb{R}$. Substituting this into the definitions of the global residual relates the change in the residual, called the first variation of \mathcal{R} and denoted as $\delta \mathcal{R}$, to the desired residual gradient by

$$\delta \mathcal{R} = \left\langle \frac{\delta \mathcal{R}}{\delta \mathbf{u}}, \epsilon \mathbf{v} \right\rangle. \quad (2.7)$$

Linearising the local residual in (2.5) and taking the adjoint of the resulting linearised operators gives the closed-form expression for the residual gradient

$$\frac{\delta \mathcal{R}}{\delta \mathbf{u}} = -\frac{\partial \mathbf{r}}{\partial t} - (\mathbf{u} \cdot \nabla) \mathbf{r} + (\nabla \mathbf{u})^\top \mathbf{r} - \frac{1}{Re} \Delta \mathbf{r} - \nabla q, \quad (2.8)$$

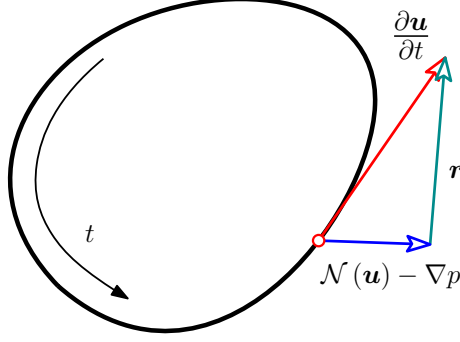


Figure 1: Schematic of an arbitrary loop in state-space that does not satisfy the governing equations as its tangent vector $\partial \mathbf{u} / \partial t$ is not aligned with the evolution operator

$$\mathcal{N} = -(\mathbf{u} \cdot \nabla) \mathbf{u} + \frac{1}{Re} \Delta \mathbf{u}.$$

with the additional constraints on the local residual

$$\nabla \cdot \mathbf{r} = 0, \quad (2.9a)$$

$$\mathbf{r}|_{y=\pm 1} = 0, \quad (2.9b)$$

as well as \mathbf{r} obeying the periodic boundary conditions. The details of the derivation for (2.8) and the source of the extra constraints in (2.9) are given in Appendix A.

The derivations described in Farazmand (2016), Azimi *et al.* (2022), and Ashtari & Schneider (2023) formulate the problem as a new set of dynamics which leads to taking the adjoint of the linearised dynamics, the primary reason that the method is typically known as the adjoint solver method rather than variational optimisation. The introduction of the new variable q in (2.8) is required to enforce the constraint that $\nabla \cdot \delta \mathcal{R} / \delta \mathbf{u} = 0$ which ensures that as the optimisation progresses the flow remains incompressible. Since q performs an identical role to the pressure p in the primitive dynamics, we call it the adjoint pressure in line with its role in Ashtari & Schneider (2023). The expression (2.8) is the same as that derived in Ashtari & Schneider (2023), with the adjoint pressure q arising as a consequence of including the continuity equation as part of the “adjoint dynamics” instead of an explicit constraint as it is treated here.

To implement a gradient-based optimisation of (2.6) it is also necessary to have a gradient of T . In this work, however, the variable $\omega = 2\pi/T$ is preferred. The variable ω is called the fundamental frequency and represents the lowest frequency oscillation that is permissible in the finite time window defined by the period T . The gradient of \mathcal{R} with respect to ω is given by

$$\frac{\partial \mathcal{R}}{\partial \omega} = \frac{1}{\omega} \left\langle \frac{\partial \mathbf{u}}{\partial t}, \mathbf{r} \right\rangle_{\Omega_t}, \quad (2.10)$$

of which the detailed derivation is given in Appendix A. Comparing (2.8) and (2.9) against (2.1) and (2.2), it can be seen that the optimisation can be viewed as a new set of “variational dynamics”, some details of which are discussed in appendix B.

2.2. Galerkin Projection

The difficulty in solving the optimisation problem in (2.6) comes from not having a simple way to compute the gradient in (2.8) while enforcing the constraints on the local residual given in (2.9). This stems from the lack of physical boundary conditions for the pressures p and q . To provide a naïve example, initialise an optimisation with a candidate field $\mathbf{u} \in \mathcal{P}_T$

with period T that does not satisfy (2.1a). To compute \mathbf{r} in (2.5), it is required to first find the pressure field p which would typically be done by solving a PPE with Neumann boundary conditions. This ensures that $\nabla \cdot \mathbf{r} = 0$, however it does not guarantee $\mathbf{r}|_{y=\pm 1} = 0$ since the Dirichlet boundary conditions are not satisfied by default, due to \mathbf{u} not representing an actual solution to the Navier-Stokes equations. The result are non-zero residual values at the wall, which invalidates the gradient $\delta\mathcal{R}/\delta\mathbf{u}$ as a guaranteed descent direction for \mathcal{R} , due to the constraints in (2.9) not being properly satisfied. In addition, the same problem exists for computing the adjoint pressure q leading to a similar problem where it is very difficult to simultaneously enforce $\nabla \cdot \mathbf{u} = 0$ and $\mathbf{u}|_{y=\pm 1} = \mathbf{u}_w$. This leads to a velocity field at the next iteration not obeying the no-slip boundary conditions. Put another way, if the system of equations that make up the variational dynamics is solved using the PPEs for p and q with standard Neumann boundary conditions, then the no-slip boundary conditions cannot be explicitly enforced and $\mathbf{u}, \mathbf{r} \notin \mathcal{P}_T$.

Ashtari & Schneider (2023) proposed a methodology for equilibrium that avoids this issue by solving for both the update to the velocity field, \mathbf{u} , and the pressure field, p , simultaneously in a coupled fashion using the IM method, which ensures that both $\nabla \cdot \mathbf{r} = 0$ and $\mathbf{r}|_{y=\pm 1} = 0$ are satisfied. The same treatment is provided for \mathbf{r} and q in a staggered approach, providing a physically consistent evolution of both \mathbf{u} and \mathbf{r} . However, as mentioned, this method was developed to solve for equilibria ($\partial/\partial t = 0$), and it is not obvious how this would work for temporally varying fields because the method used to obtain compatible velocity and pressure fields is designed as an update method for some time-stepping scheme.

With the difficulties in evolving the variational dynamics while satisfying all the constraints now clear, we propose to use a Galerkin projection onto an orthogonal basis that satisfies the boundary conditions and the incompressibility constraints. Some setup is required to arrive at the final procedure that yields a valid computation of the residuals and gradient that obey the constraints. First, the velocity field is expanded into a sum over a basis as follows

$$\mathbf{u}(x, y, z, t) = \mathbf{u}_b + \sum_{i=1}^{\infty} \sum_{\mathbf{k} \in \mathbb{Z}^3} a_{\mathbf{k}i} \psi_{\mathbf{k}i}(y) e^{i\mathbf{k} \cdot \boldsymbol{\xi}}, \quad (2.11)$$

where $\mathbf{k} = (k_x \ k_z \ k_t)^\top$ is the integer wavenumber vector, and $\boldsymbol{\xi} = (\alpha x \ \beta z \ \omega t)^\top$ is the scaled direction vector. The coefficients $\alpha = 2\pi/L_x$, $\beta = 2\pi/L_z$, and $\omega = 2\pi/T$ are determined by the domain size and period of the flow, and each represent the smallest frequency in each of their respective direction that can be accommodated in the finite space. The modes $\psi_{\mathbf{k}i} = \psi_{\mathbf{k}i}(y)$ are divergence-free and obey the no-slip boundary conditions

$$\nabla_{\mathbf{k}} \cdot \psi_{\mathbf{k}i} = 0, \quad (2.12)$$

$$\psi_{\mathbf{k}i}|_{y=\pm 1} = 0, \quad (2.13)$$

in addition to being orthonormal

$$\int_{-1}^1 \psi_{\mathbf{k}i}^\dagger \cdot \psi_{\mathbf{k}j} dy = \delta_{ij}. \quad (2.14)$$

where δ_{ij} is the Kronecker delta, and $(\cdot)^\dagger$ denotes the conjugate transpose. The operator $\nabla_{\mathbf{k}} \cdot = i\alpha k_x + \partial/\partial y + i\beta k_z$ is the divergence operator in spectral/Fourier space. To account for the inhomogeneous boundary conditions on \mathbf{u} , the steady base flow $\mathbf{u}_b = \mathbf{u}_b(y)$ is introduced into (2.11). The sum over the set of modes $\psi_{\mathbf{k}i}$ is taken over a countably infinite set of modes for every frequency \mathbf{k} to form a complete basis for the optimisation space \mathcal{P}_T . In practice, when the problem is discretised or when forming a reduced-order model of the dynamics, this sum is truncated to a finite number denoted with $M \in \mathbb{N}$. The key observation is that for any combination of coefficients $a_{\mathbf{k}i} \in \mathbb{C}$ the velocity field is incompressible and

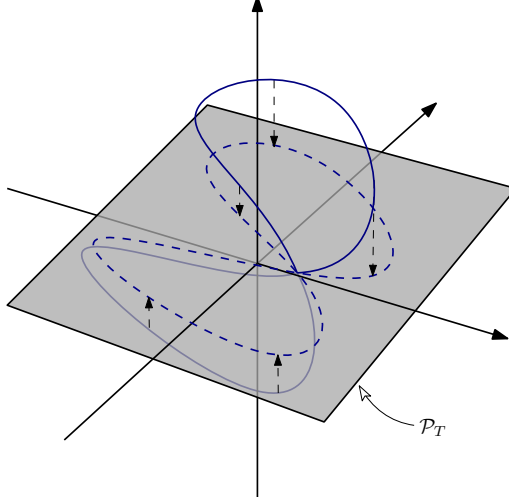


Figure 2: Schematic for a Galerkin projection of state-space loop representing a velocity field onto the linear subspace in (2.4).

obeys the no-slip boundary conditions, restricting the velocity field to exist only within a finite-dimensional sub-space of the complete function space.

The orthogonality of the modes allows for the following identity for the coefficients a_{ki} to be derived

$$a_{ki} = \frac{1}{2TL_zL_x} \langle \mathbf{u} - \mathbf{u}_b, e^{-ik \cdot \xi} \psi_{ki} \rangle_{\Omega_t} \quad (2.15)$$

This projection is least-squares, in the sense that the set of coefficients a_{ki} produces a trajectory that is the closest possible trajectory to \mathbf{u} restricted to be within the linear subspace defined by ψ_{ki} . A low-dimensional schematic for such a projection is depicted in figure 2.

Next, a similar expansion can be performed for the local residual

$$\mathbf{r} = \sum_{i=1}^{\infty} \sum_{\mathbf{k} \in \mathbb{Z}^3} s_{ki} \psi_{ki}(\mathbf{y}) e^{ik \cdot \xi}, \quad (2.16)$$

Similar to (2.11), any combination of coefficients $s_{ki} \in \mathbb{C}$ constructs a local residual field that obeys the constraints (2.9), making it the crucial step in this methodology. The coefficients s_{ki} can be computed in a similar way as to velocity

$$s_{ki} = \langle \mathbf{r}, e^{ik \cdot \xi} \psi_{ki} \rangle_{\Omega_t}. \quad (2.17)$$

If the expansions (2.11) and (2.16) are substituted into (2.8) and (2.5), and the results are projected using the same operation as in (2.15) we get the following expressions for the gradient of \mathcal{R} with respect to the coefficients a_{ki}

$$\frac{\partial \mathcal{R}}{\partial a_{ki}} = -ik_t \omega s_{ki} - \left\langle (\mathbf{u} \cdot \nabla) \mathbf{r} - (\nabla \mathbf{u}^\top) \mathbf{r} + \frac{1}{Re} \Delta \mathbf{r}, e^{-ik \cdot \xi} \psi_{ki} \right\rangle_{\Omega_t}, \quad (2.18)$$

and for the local residual coefficients s_{ki}

$$s_{ki} = ik_t \omega a_{ki} + \left\langle (\mathbf{u} \cdot \nabla) \mathbf{u} - \frac{1}{Re} \Delta \mathbf{u}, e^{-ik \cdot \xi} \psi_{ki} \right\rangle_{\Omega_t}. \quad (2.19)$$

The key observation to be made on the expressions (2.18) and (2.19) is that the pressure

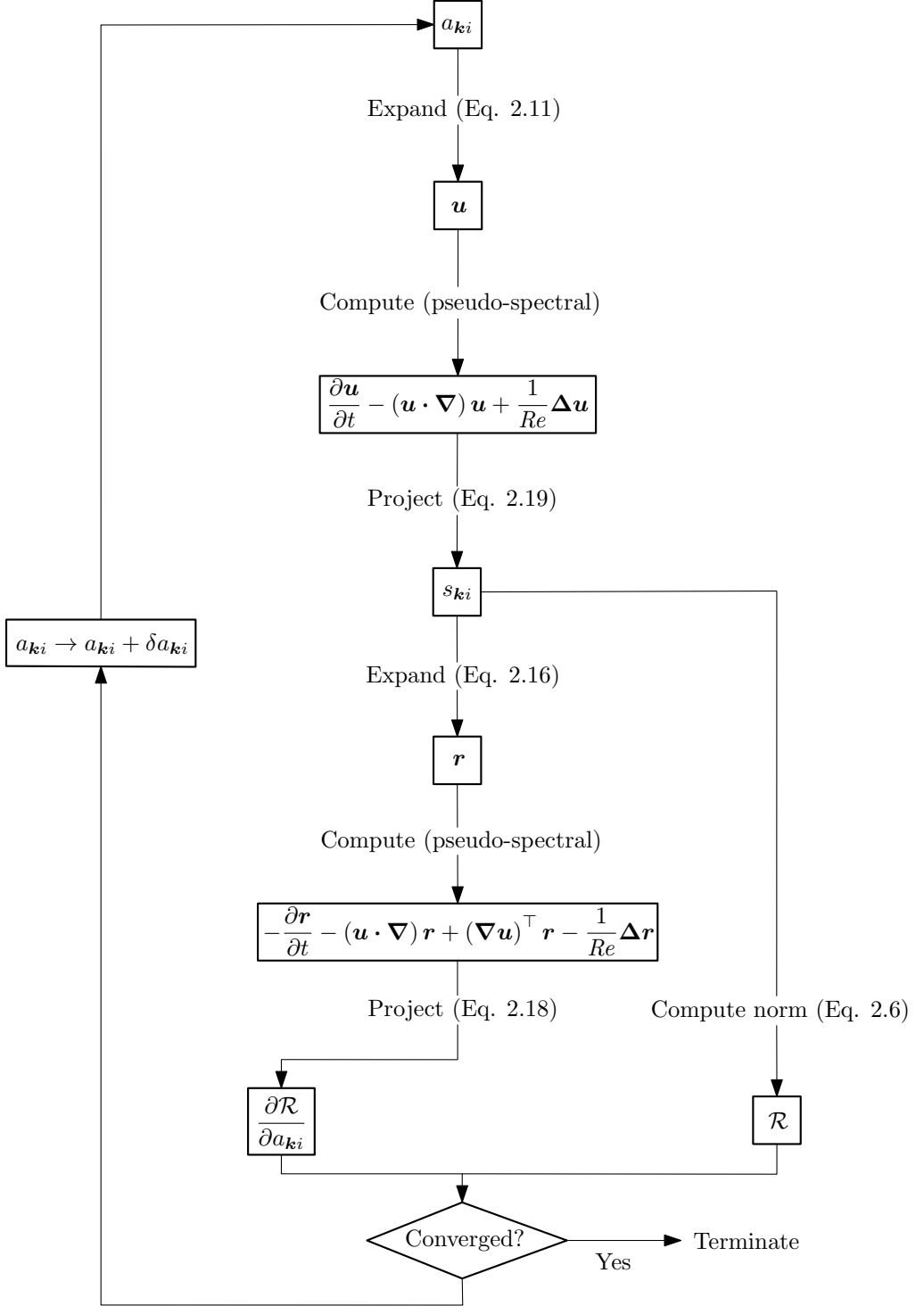


Figure 3: Flow diagram of the computations performed at each iteration of the optimisation.

gradient terms are not present. This is a result of the fact the basis ψ_{ki} is divergence-free, leading to the following result

$$\langle \nabla p, e^{-ik \cdot \xi} \psi_{ki} \rangle_{\Omega_t} = \left\langle p, \nabla \cdot \left(e^{-ik \cdot \xi} \psi_{ki} \right) \right\rangle_{\Omega_t} = \langle p, e^{-ik \cdot \xi} \nabla_k \cdot \psi_{ki} \rangle_{\Omega_t} = 0, \quad (2.20)$$

and similarly for the adjoint pressure gradient term ∇q .

Figure 3 is a flow diagram for the data over a single iteration of a given optimisation loop, to compute both \mathcal{R} and $\partial \mathcal{R} / \partial a_{ki}$. The computation begins with the coefficients a_{ki} that represent a given periodic and incompressible velocity field that obeys the periodicity and no-slip boundary conditions, relative to a given set of modes ψ_{ki} and base flow u_b . The residual coefficients s_{ki} are then obtained by computing all the terms in (2.5) excluding the pressure gradient ∇p , the result of which is then projected onto the basis as in (2.17). The global residual can be obtained directly from s_{ki} . To obtain the residual gradient, the velocity and residual coefficients are expanded back into physical space to facilitate the computation of all the terms on the right-hand side of (2.8) excluding the adjoint pressure gradient ∇q . Finally the result is projected using (2.18) to obtain $\partial \mathcal{R} / \partial a_{ki}$. With both \mathcal{R} and its gradient, the chosen optimisation algorithm can be used to update the coefficients a_{ki} to reduce \mathcal{R} , with convergence being determined by the size of \mathcal{R} . The process summarised here allows the direct computation of the required residual and gradient without resorting to solving a PPE, avoiding the issues related to the boundary conditions. The frequency gradient $\partial \mathcal{R} / \partial \omega$ does not require any extra special treatment as once the appropriate local residual r has been determined then (2.10) can be computed directly.

It should be noted that the spatial derivative terms in (2.18) and (2.19) are not explicitly computed in terms of the coefficients a_{ki} and s_{ki} here. These expressions would depend on the explicit form of the modes ψ_{ki} as could be seen by substituting the expansions (2.11) and (2.16) into (2.18), and thus a general statement cannot be provided. In addition, the computation of the nonlinear terms in projected space using a_{ki} and s_{ki} would be in the form of several convolution sums, as can be seen in Barthel *et al.* (2021). These sums scale very poorly with the degrees-of-freedom of the system, and for this reason a pseudo-spectral approach is taken. The velocity and residual are expanded back into their full physical space forms where the nonlinear terms are computed after which they are then projected back onto the modes. This avoids the heavy computation of convolutional sums in the reduced-order space, replacing them with pointwise multiplication in physical space. Truncating the number of modes used in the expansion/projection steps of the procedure to a potential small number of dynamically significant modes forms a low-order model for the dynamics. This low-order model is characterised by the shape of the modes ψ_{ki} and the number of modes retained. The primary effects of this truncation are discussed in section 6.

3. Resolvent Analysis

To implement the projected variational optimisation methodology, a method to generate the modes ψ_{ki} with the desired properties (2.12)-(2.14) is required. This choice is non-trivial with many possible solutions. For example, SPOD could be used to generate a set of modes from large data sets, or global stability analysis can derive modes directly from the Navier-Stokes equations. Here resolvent analysis is used to generate the desired modes, and for completeness we provide an overview of resolvent analysis following closely the formulation provided in Sharma (2019).

First, decompose the velocity field into a steady base component and the fluctuation around this base flow as follows

$$u(x, y, z, t) = u_b(x, y, z) + u'(x, y, z, t), \quad (3.1)$$

where the base flow here is distinct from the one used in (2.11). The standard choice in resolvent analysis is to take \mathbf{u}_b to be the turbulent mean. The choice taken in this work is different for primarily pragmatic reasons and is discussed further in sections 5 and 6.

At this point it is useful to define the Leray projector $\mathbb{P}\mathbf{u} = \mathbf{u} - \nabla\Delta^{-1}(\nabla \cdot \mathbf{u})$ Temam (1984). This operator takes an instantaneous velocity field and orthogonally projects onto the divergence-free subspace, and can be derived from Helmholtz decomposition of the velocity field. Applying the Leray projector to (2.1a) and then substituting in the decomposition (3.1) provides an evolution equation for the fluctuations

$$\frac{\partial \mathbf{u}'}{\partial t} = \mathbb{P} \left(\mathcal{N}(\mathbf{u}_b) + \mathcal{L}_{\mathbf{u}_b} \mathbf{u}' + \mathbf{f}(\mathbf{u}') \right). \quad (3.2)$$

The operator $\mathcal{N}(\mathbf{u})$ is the Navier-Stokes operator, given by the right-hand side of (2.1a). The operator $\mathcal{L}_{\mathbf{u}_b}$ is the linearised Navier-Stokes operator evaluated at the base flow \mathbf{u}_b . Finally, $\mathbf{f}(\mathbf{u}') = -(\mathbf{u}' \cdot \nabla) \mathbf{u}'$ is the nonlinear term for the fluctuations \mathbf{u}' . Physically \mathbf{f} the nonlinear feedback that transports energy between scales and sustains any unsteady motion in the flow. The addition of the Leray projector allows us to ignore the pressure gradient terms in the operators \mathcal{N} and $\mathcal{L}_{\mathbf{u}_b}$, as well as not needing to explicitly represent the continuity equation in (3.2).

Next we define the Fourier expansion of the velocity fluctuation \mathbf{u}' in the homogeneous spatial and time directions as follows, following closely the formulation used in section 2.2,

$$\mathbf{u}'(x, y, z, t) = \sum_{\mathbf{k} \in \mathbb{Z}^3} \mathbf{u}'_{\mathbf{k}}(y) e^{i\mathbf{k} \cdot \boldsymbol{\xi}}, \quad (3.3)$$

where \mathbf{k} and $\boldsymbol{\xi}$ have the same definition as in section 2.2. The corresponding inverse operation to compute the Fourier coefficients is given by

$$\mathbf{u}'_{\mathbf{k}} = \frac{1}{4\pi^2} \int_0^{2\pi} \int_0^{2\pi} \int_0^{2\pi} \mathbf{u}' e^{i\mathbf{k} \cdot \boldsymbol{\xi}} d\boldsymbol{\xi}. \quad (3.4)$$

Expanding (3.2) into its Fourier coefficients the following is obtained for the fluctuations

$$ik_t \omega \mathbf{u}'_{\mathbf{k}} = \mathbb{P} \left(\mathcal{L}_{\mathbf{k}, \mathbf{u}_b} \mathbf{u}'_{\mathbf{k}} + \mathbf{f}_{\mathbf{k}} \right), \quad \mathbf{k} \in \mathbb{Z}^3 \setminus \{\mathbf{0}\}. \quad (3.5)$$

Rearranging, one obtains the following linear relationship between the fluctuations and the nonlinear interactions resulting from the convective term.

$$\mathbf{u}'_{\mathbf{k}} = \mathbf{R}_{\mathbf{k}} \mathbf{f}_{\mathbf{k}}, \quad \mathbf{k} \in \mathbb{Z}^3 \setminus \{\mathbf{0}\}. \quad (3.6)$$

The operator $\mathbf{R}_{\mathbf{k}} = (ik_t \omega \mathbf{I} - \mathbb{P} \mathcal{L}_{\mathbf{k}, \mathbf{u}_b})^{-1} \mathbb{P}$ is the resolvent. The exact form of $\mathbf{R}_{\mathbf{k}}$ is given in appendix C. The next step is to decompose the operator using a Schmidt decomposition, or equivalently a Singular Value Decomposition (SVD) when discretised, as follows

$$\mathbf{R}_{\mathbf{k}}(\cdot) = \sum_{i=1}^{\infty} \sigma_{ki} \boldsymbol{\psi}_{ki} \langle \boldsymbol{\phi}_{ki}, \cdot \rangle. \quad (3.7)$$

This decomposition provides two sets of orthonormal modes, i.e.

$$\int_{-1}^1 \boldsymbol{\psi}_{ki}^{\dagger} \boldsymbol{\psi}_{kj} dy = \delta_{ij}, \quad (3.8)$$

$$\int_{-1}^1 \boldsymbol{\phi}_{ki}^{\dagger} \boldsymbol{\phi}_{kj} dy = \delta_{ij}, \quad (3.9)$$

ranked in order of the associated singular values $\sigma_i \geq \sigma_{i+1} \geq 0$, for all $i \in \mathbb{N}$. The modes

ψ_{ki} and ϕ_{ki} are the left and right singular modes and form a complete basis for the range (response) and domain (input) of the resolvent for every $\mathbf{k} \in \mathbb{Z}^3 \setminus \{0\}$, respectively.

To actually find exact solutions as discussed in section 2, a basis for the mean $\mathbf{k} = 0$ is also required. The resolvent in (3.6) is only technically defined using the fluctuation equation at all non-zero frequencies, $\mathbf{k} \neq 0$, however the resolvent operator can regardless be evaluated at $\mathbf{k} = 0$. The exact physical interpretation of the basis used for the Galerkin projection is less important as its ability to provide a valid orthonormal basis in the space of divergence-free and no-slip fields. The literature discussing the evaluation of the resolvent at the mean frequencies and wavenumbers is extremely sparse, since it is not typically required as the mean is used as an input. The exception is Mons & Marquet (2021) which uses resolvent of the RANS for the purpose of data assimilation.

Since the range of the resolvent is the space of divergence-free fluctuation velocity fields that obey the desired boundary condition, the left singular modes, ψ_{ki} , also called the response modes, have these desired properties. Thus, the response modes ψ_{ki} can be used as the basis for the Galerkin projection introduced in section 2.2.

The rate at which the singular values σ_i decay determines how accurately the decomposition (3.7) can be represented with only a finite number of the modes. It has been observed for fluid flows that the singular values decay rather rapidly (McKeon & Sharma 2010), meaning a low-rank approximation to the resolvent operator can be constructed with a partial sum of (3.7). This reduces the dimensionality of the amplification mechanisms in (3.6), only keeping the most significant contributions.

4. General Features of Rotating Plane Couette Flow

We now introduce RPCF, defining the governing equations for this flow, as well as its general features and normal solutions at various regimes. Figure 4 is a diagram of the flow geometry between two parallel plates moving in opposite directions in a reference rotating around the spanwise direction.

The governing equations for this flow are given by

$$\frac{\partial \mathbf{u}}{\partial t} = -(\mathbf{u} \cdot \nabla) \mathbf{u} - \nabla p + \frac{1}{Re} \Delta \mathbf{u} - Ro (\hat{\mathbf{k}} \times \mathbf{u}), \quad (4.1a)$$

$$\nabla \cdot \mathbf{u} = 0. \quad (4.1b)$$

with the (normalised) boundary conditions at the wall

$$\mathbf{u}|_{y=\pm 1} = \pm 1, \quad (4.2)$$

in addition to the periodicity boundary conditions in the streamwise and spanwise directions. In this work we make an additional assumption that the flow is streamwise-independent ($\partial/\partial x = 0$) reducing it to a 2-Dimensional 3-Component (2D3C) formulation. The primary reason to use a 2D3C formulation of the flow is to reduce the dimensionality of the problem making the solutions easier to find while retaining many of the key features of the original dynamics. This constraint in fact makes the flow exactly analogous to Rayleigh-Benard convection as shown in (Eckhardt *et al.* 2020). The analogy between rotating shear flows and convective thermal flows has been known for some decades (Chandrasekhar 1961; Yih 1965), and has been used to describe Taylor-Couette flows in turbulent regimes in relation to the Rayleigh Benard convection (Eckhardt *et al.* 2007). The nature of some steady and streamwise-independent solutions to the RPCF at low Reynolds numbers (before bifurcating into more complex structures) is discussed in Nagata (2013); Nagata *et al.* (2021).

The streamwise-independence means that the domain size of the flow is given solely by the half-channel height h and the spanwise length L_z , with the aspect ratio defined as the ratio

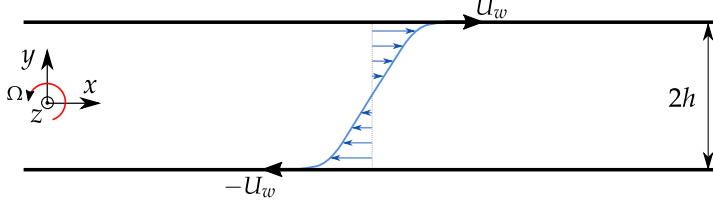


Figure 4: Schematic for the rotating plan Couette flow with nomenclature.

$\gamma = L_z/h$. In this work an aspect ratio of $\gamma = 4$ is used exclusively, which is equivalent to setting $L_z = 8$. The flow is characterised by two non-dimensional parameters, the Reynolds number Re and Rotation number Ro defined as

$$Re = \frac{U_w h}{\nu}, \quad Ro = \frac{2\Omega h}{U_w}, \quad (4.3)$$

where U_w is the wall speed, ν is the kinematic viscosity, and Ω is dimensional rotation rate. The Rotation number is the ratio between the characteristic rotation and inertial forces of the system. In this work only the case of the rotation being oriented to point out of the page is considered. This is known as anti-cyclonic rotation and acts to produce linear instabilities at finite Reynolds numbers (Tsukahara *et al.* 2010), as opposed to standard plane Couette flow that is linearly stable for all finite Reynolds numbers (Daviaud *et al.* 1992). In general, the most interesting parameter range for the Rotation number is $0 < Ro < 1$ as this is range that destabilises the flow. For any value outside this range for Ro , the flow is actually made more linearly stable by the presence of system rotation (Lezius & Johnston 1976; Hiwatashi *et al.* 2007).

The flow starts as with a stable laminar solution that is identical that of plane Couette flow. Linear stability analysis shows the boundary of stability for the laminar flow has the following relationship

$$Re = \sqrt{\frac{107}{Ro(1 - Ro)}}, \quad (4.4)$$

given in Lezius & Johnston (1976). This initial bifurcation of the fully 3D flow leads to a streamwise flow, and so it is also a valid relation for the 2D3C case. This implies that the laminar flow is most unstable for $Ro = 0.5$, which is the rotation number of choice for this work. At $Re \approx 20.7$ the laminar state bifurcates and becomes unstable. A new stable equilibrium solution is born out of this bifurcation which has the characteristic streamwise-independent rolls that are present throughout the total set of regimes accessible by varying Re .

We characterise the transition behaviour by analysing the kinetic energy extrema, defined as $\mathcal{K}(t) = \frac{1}{2} \|\mathbf{u}(t)\|_{\Omega}$, of the DNS data over a range of Reynolds numbers at $Ro = 0.5$. The results are shown in figure 5. This and any further DNS results shown in this work were obtained using a custom solver originally developed for Lasagna *et al.* (2016) using a vorticity-streamfunction formulation of the flow. The data for figure 5 was obtained by simulating a random initial condition at the given Reynolds number for long enough to ensure the simulation has converged to the final attractor, typically taking of the order of thousands of time units. A full analysis of the transitional behaviour of 2D3C RPCF is beyond the scope of this work. However, there are some key features in figure 5 that it will be useful to further discuss. As the Reynolds number is further increased above the laminar bifurcation the streamwise rolls grow in strength. This continues until the equilibrium flow becomes unstable enough to yield to a periodic flow. The exact bifurcation that occurs is

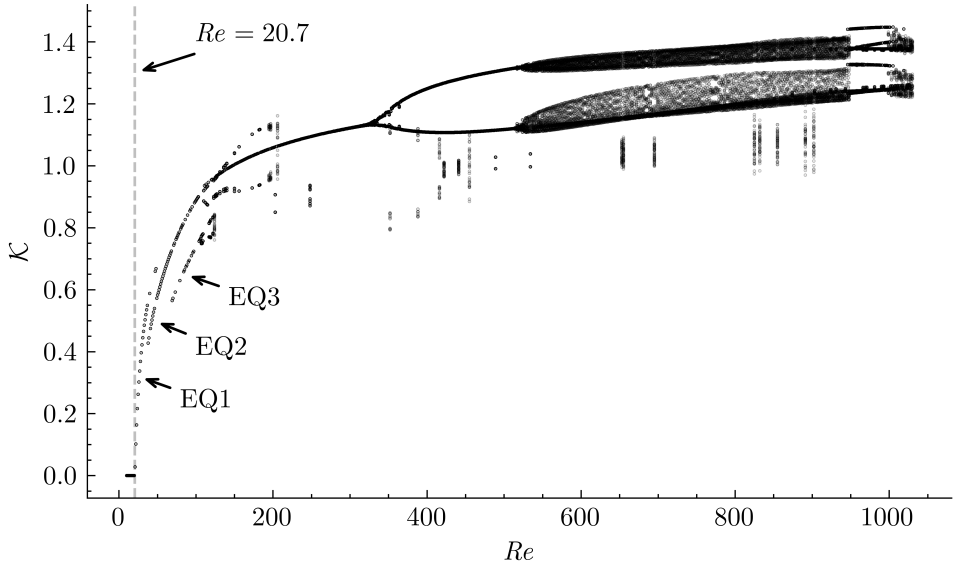


Figure 5: Bifurcation diagram of RPCF over a range of Reynolds number and $Ro = 0.5$ showing the transition from the stable laminar solution to turbulent flow.

rather complex, with a stable equilibrium and periodic solution seemingly existing at the same time for certain ranges of Reynolds numbers. Once the Reynolds number has reached about $Re = 350$, the DNS converge towards a single periodic solution. The spatial structure of this stable periodic solution does not differ much from the equilibrium, with the majority of the kinetic energy being stored in large streamwise rolls. This stable periodic orbit gradually gives way to more complex non-periodic behaviour. Eventually, the flow reaches a point where the flow has become sufficiently complex to be considered turbulent, with a broadband spectrum and notable separation of scales.

The initial bifurcation from the laminar state occurs at the expected value predicted from (4.4) and the kinetic energy of the new stable equilibrium grows quickly. Notably, instead of the single equilibrium being traced continuously as the Reynolds number increases the favoured attractor the DNS settles on changes. These new branches represent alternative stable equilibrium solutions. The equilibrium solutions at $Re = 50$ for each branch labelled in figure 5 are shown in figure 6. These solutions are labelled as S1, S2, and S3, as depicted in figure 5. The solutions of each branch differ primarily in the number of streamwise rolls. The solutions have kinetic energies of $\mathcal{K} \approx 0.65$, $\mathcal{K} \approx 0.58$, and $\mathcal{K} \approx 0.39$, for S1-3 respectively. The denser the rolls the lower the kinetic energy as a result of the higher dissipation rates at the same Reynolds number. Also of note is that the higher the Reynolds number the more favoured the denser rolling structures become, likely as a result of the previous branch not being able to sustain the required dissipation rates to produce a stable equilibrium. It should be noted that all of these solutions are linearly stable at $Re = 50$ as the DNS converged towards each of them as long as the initial condition is sufficiently close. The primary reason for some the branches, especially S3, not being observed at this Reynolds number is likely due to a small basin of attraction at $Re = 50$.

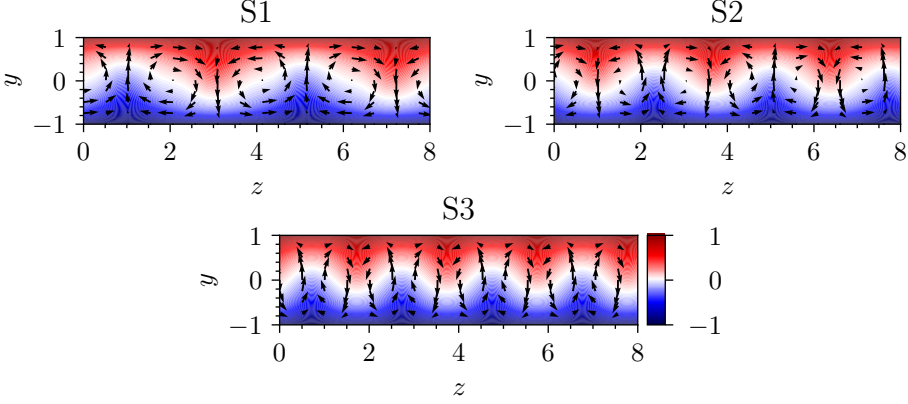


Figure 6: Equilibrium solutions for branch shown in figure 5 in the Reynolds range of $20 \lesssim Re \lesssim 100$.

5. Exact Solutions Found for RPCF

In this section the focus is a demonstration of the projected variational optimisation methodology applied to finding exact nonlinear solutions to the Navier-Stokes equations for RPCF. These solutions are obtained by providing a sufficiently large number of resolvent modes to the optimiser, such that basis can be considered complete. With this complete basis the global residual as defined in (2.6) can be made very small.

5.1. Implementation Details

This section discusses the numerics and programmatic strategies used to implement the procedure depicted in figure 3. All of the numerics are implemented in the Julia programming language with the majority of the code available at [The-ReSolver](#). A single spatially and temporally extended scalar field is represented as a 3D array, with each dimension representing the wall-normal, spanwise, and time directions, respectively. The number of wall-normal points, spanwise points, and number of temporal samples are denoted by N_y , N_z , and N_t , respectively. Since the physical field is represented a real FFT transformed array the actual array has dimension of $N_y \times (\lfloor N_z/2 \rfloor + 1) \times N_t$, where $\lfloor \cdot \rfloor$ denotes the integer floor operation. The spanwise and time directions are transformed using FFTs (Frigo & Johnson 2005), and so the discretisations in these directions are necessarily uniform. The distribution of wall-normal points is not restricted to be uniform since this direction is not represented with a Fourier transform. However, they are typically also uniform to allow easy interoperability with the DNS and Julia codes. The resolvent modes are represented by a 4D array, the extra dimension corresponding to multiple modes being available at each frequency and wall-normal location. The modal coefficients a_{ki} (and s_{ki}) are represented very similarly in the program, only with the array dimension corresponding to the wall-normal direction now representing the modal index i , with a length M for the number of modes used for the projection in (2.15) and (2.17). The storage of multiple fields with their complete time history, as well as the set of modes being used, represents the vast majority of the memory requirements of the programme. This problem is highly parallelisable due to the global representation, which is likely a necessary step to implementing these methods for fully 3D problems or for higher Reynolds numbers.

Derivatives in the spanwise and time directions can be computed using standard spectral methods. Derivatives in the wall-normal direction are computed using finite difference methods, generally of fourth order accuracy. The finite difference stencils are derived using

the custom package [FDGrids.jl](#). To compute the projection in (2.15) and (2.17) it is necessary to compute integrals over all the directions given the definition of the inner-product in (2.3). In the spanwise and time directions this can be done by using Parseval's theorem, converting the integral over these directions to sums of the coefficients over the corresponding wavenumbers. The wall-normal integrals are computed using the method of undetermined coefficients for quadratures (Dahlquist & Björck 2008). The nonlinear terms in the computations are computed using a pseudo-spectral method, using a 3/2 padding rule in the spanwise and time directions to avoid aliasing errors.

When constructing the modes ψ_{ki} using resolvent analysis, the base flow used is the laminar solution $\mathbf{u}_b = y\hat{\mathbf{i}}$. This choice is made for its computational simplicity and numerical robustness; the laminar base flow is well-defined, analytically simple, and guarantees a tractable, well-conditioned singular value decomposition for all wavenumbers $\mathbf{k} \in \mathbb{Z}^2$ (including $\mathbf{k} = 0$). Consequently, it provides a reliably calculable set of modes ψ_{ki} without requiring a priori knowledge of the flow or introducing the numerical complications associated with a turbulent mean profile. For the computation of the SVD, the divide and conquer algorithm is used.

We are free to choose the optimisation algorithm used for solving the optimisation problem (2.6), since any gradient-based method will work. Unless otherwise stated, L-BFGS is the algorithm used here. L-BFGS is a quasi-Newton method, incorporating approximate Hessian information into each iteration, which significantly improves the convergence properties of the optimisation near minima compared to gradient descent. This is particularly important here because the optimisation problem is non-convex, with many possible solutions potentially very close together. The problem is also generally quite poorly conditioned, mostly due to the influence of the Laplacian which has large effects on the high frequency components of the flow that decay away the most rapidly. L-BFGS's ability to approximate the local curvature of the solution reduces the effect of this poor conditioning. Further discussions on each algorithm can be found in Nocedal & Wright (2006). The optimisation is performed using the [Optim.jl](#) package (Mogensen & Riseth 2018). Any algorithm used here is also coupled with the Hager-Zhang line search algorithm as described in Hager & Zhang (2005). This further improves convergence rates, albeit at the possibility of reducing the robustness of the convergence. In practice, however, this is not observed to be an issue. The threshold for convergence is defined as $\mathcal{R}[\mathbf{u}] < 10^{-12}$.

5.2. Equilibria

The Reynolds number to $Re = 50$ and Rotation number $Ro = 0.5$ for the equilibrium solutions. To begin, the optimiser is validated by observing its ability to reconstruct a known solution to the flow. This was obtained using the custom DNS solver, using a grid discretisation of $N_y = 64$ on a uniform grid, and $N_z = 32$ corresponding to 17 spanwise Fourier modes. A set of $M = 64$ resolvent modes ψ_{ki} are used for this optimisation. To obtain the initial guess for the start of the optimisation S1 from DNS in figure 6 is projected onto the resolvent basis and then perturbed with random Gaussian white noise at each coefficient a_{ki} . This results in the highly disordered field in figure 7(a). This perturbed flow is then optimised to try to recover the original solution. The result of this optimisation is shown in figure 7(b). This can be compared to S1 in figure 6, where the equilibria from the DNS and optimisation are qualitatively indistinguishable. Figure 7(c) shows the difference between the solution obtained from optimisation and from the DNS. The magnitude of the difference is a couple of orders magnitude smaller than that of the actual solution. The majority of the difference between the solutions is going to be a result of the differing numerics used in the DNS solver and Julia optimiser. This validates the optimiser possesses minima that correspond to solutions of (4.1).

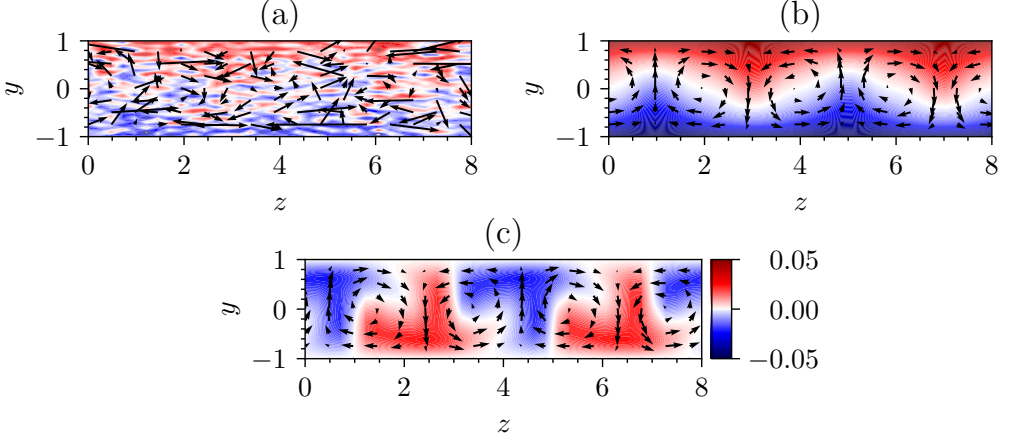


Figure 7: Snapshots of the flows before and after the optimisation at $Re = 50$ and $Ro = 0.5$, along with the solution obtained from DNS. Panel (a) shows the initial flow used for the optimisation, obtained by perturbing the stable solution obtained from DNS at the same Reynolds and Rotation numbers. Panel (b) shows the result of the optimisation with a residual of $\mathcal{R} < 10^{-12}$, and panel (c) is difference between the optimisation result and the DNS solution.

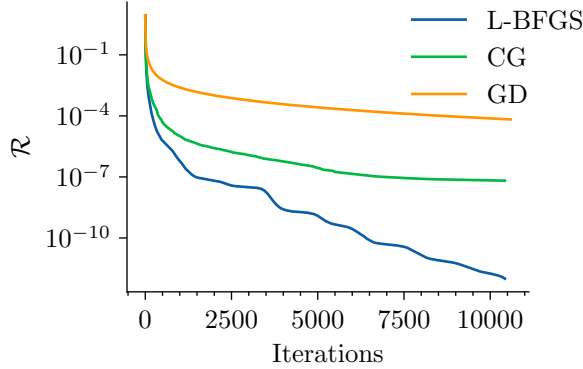


Figure 8: Residual trace for the optimisation of the initial flow given in panel (a) of figure 7, using Gradient Descent (GD), Conjugate Gradient (CG), and L-BFGS optimisation algorithms. All solutions converge towards the solution obtained in panel (b) of figure 7.

For comparison, the same initial condition was also optimised using the gradient descent and conjugate gradient algorithms (both still using Hager-Zhang line searches). The traces for each algorithm applied to the initial condition in figure 7(a) are shown in figure 8. Clearly L-BFGS performs the best, achieving the residual of $\mathcal{R} = 10^{-12}$ after roughly 10000 iterations. Gradient descent displays an initial large decrease in residual which quickly decreases as the convergence rate slows. This slow convergence rate is primarily due to the poor conditioning of the optimisation. Conjugate gradient also outperforms gradient descent, achieving a smaller residual for the same number of iterations. However, after the initial large decrease in the residual at the beginning of the optimisation, the convergence rate slows, approaching a similar speed as gradient descent. In addition, the iteration time of conjugate gradient is observed to be larger than L-BFGS.

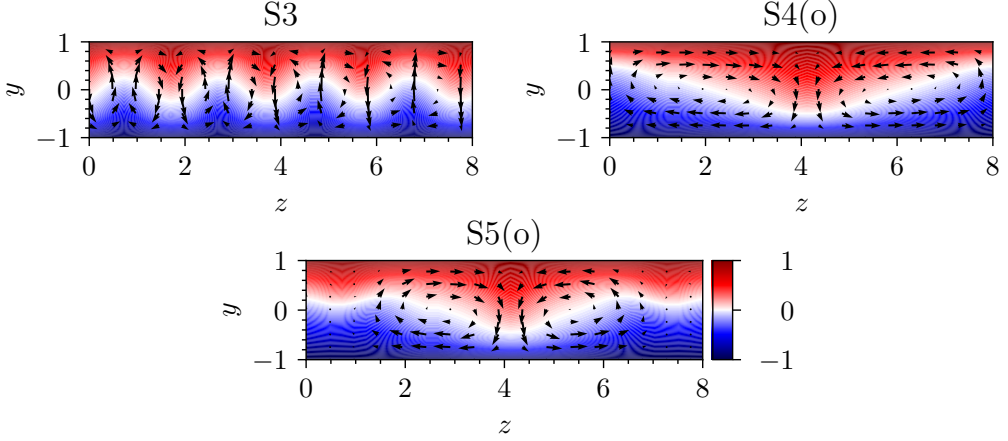


Figure 9: Final snapshots of the solutions obtained by optimising from various synthetic initial flow fields.

To investigate the robustness of the optimiser, it was initialised with various of initial conditions exciting certain spanwise wavenumbers with the intent of finding multiple new equilibrium solutions that are not observed in DNS of the flow at this Reynolds number. The same set of resolvent modes used for the previous optimisation are utilised here. The results of these optimisations are shown in figure 9. Figure 9(a) was initialised with the first 5 modal coefficients a_{ki} excited with random values at the spanwise wavenumber of $k_z = 4$, corresponding to streamwise rolls with half the wavelength of S1, with the rest of the coefficients left as zero. This converges to S3, one of the stable equilibrium shown in figure 6. Next the first 5 modal coefficients are excited randomly for the spanwise wavenumber $k_z = 1$, the solution in figure 9(b) is found, called S4(o). The addition of “(o)” in the name given to the equilibrium is in reference to the fact that it has been obtained from optimisation and is not a solution observed from the DNS. This solution again has the streamwise roll expected from the other equilibria solutions, but now with twice the spanwise wavelength. The highly symmetric structures of S3 and S4(o) closely mirror the solution of S1, and is ultimately expressing the same dynamics. To obtain a slightly more abnormal solution, the flow was initialised by exciting the first 8 resolvent modes at the zeroth and first ($k_z = 0, 1$) spanwise wavenumbers with random values. The result of optimising such an initial condition is shown in figure 9(c), called S5(o). S5(o) shows a streamwise roll pattern with a width larger than in S1, roughly 3 spanwise units in length. This roll does not repeat over the remaining length of the domain since there is not sufficient room. Instead, the flow remains mostly stagnant in the remaining space, only expressing some very weak rolls that transports a small amount of the momentum from the top wall downwards.

The spanwise power spectra of the intermediate flow over the duration of the optimisation leading to S3 are shown in figure 10. For clarity, the wavenumbers that are orders of magnitude smaller than those shown are filtered out. The filtered wavenumbers have negligible impact on the solution and are primarily a result of the spanwise domain size being large enough to contain multiple repetitions of the fundamental unit of the solution. The initial field used for the optimisation was excited at exactly one spanwise wavenumber, $k_z = 4$. The optimiser initially increases the spectral power at the harmonic (and mean) wavenumbers as can be seen at iteration $i = 20$, which is then followed by a gradual process of distributing the energy out from the higher wavenumbers until it settles on the final spectral peaks.

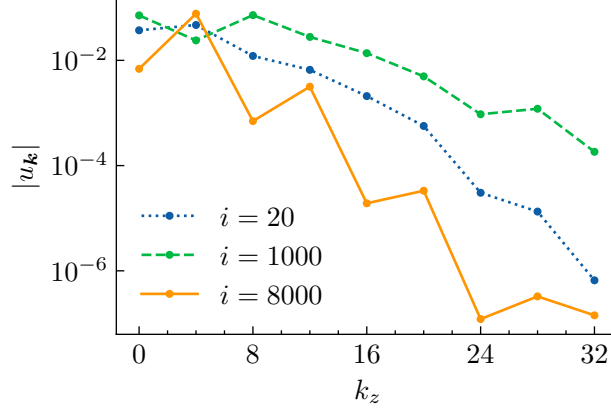


Figure 10: Spanwise power spectra of S3 of the solutions obtained at specific iterations of its optimisation, sampled at the channel midpoint ($y = 0$).

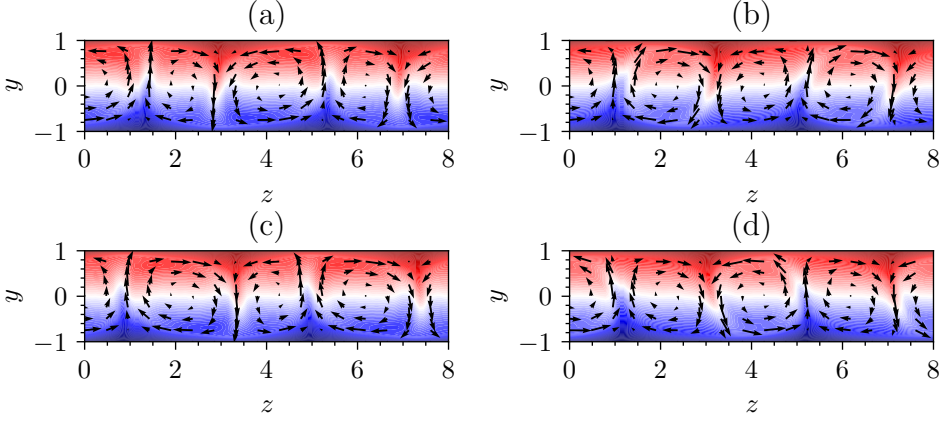


Figure 11: Snapshots of the periodic solution ($\mathcal{R} \approx 5 \times 10^{-13}$) obtained for $Re = 400$ with a period of $T \approx 25.07$. Panel (a) shows $t = 0$, panel (b) shows $t = T/4$, panel (c) shows $t = T/2$, and panel (d) shows $t = 3T/4$.

5.3. Periodic Solutions

The optimiser is now tasked with constructing a periodic solution at $Re = 400$, a regime where RPCF displays a stable periodic motion as seen in figure 5. The flow is discretised with $N_y = 128$, $N_z = 64$, corresponding to 33 spanwise modes, and $N_t = 35$ temporal modes. A set of $M = 64$ resolvent modes for each frequency are used for the optimisation. The smaller number of resolvent modes is used primarily to reduce computational effort. As will be seen in this section, the reduced number of modes compared to the degrees-of-freedom in the wall-normal direction have little effect on the accuracy of the final result. The initial guess for the optimiser is initialised in a similar way as in the first validation case in section 5.2. The periodic DNS data at $Re = 400$ is projected onto the resolvent modes. The resulting coefficients a_{ki} are then perturbed with random Gaussian white noise. The resulting noisy flow is optimised.

Figure 11 shows a set of snapshots for the periodic solution obtained from optimisation at $Re = 400$, sampled at points along its trajectory. The primary streamwise rolls are clearly present, and evolve in a wavy motion as consecutive vortices contract and expand. Figure 12

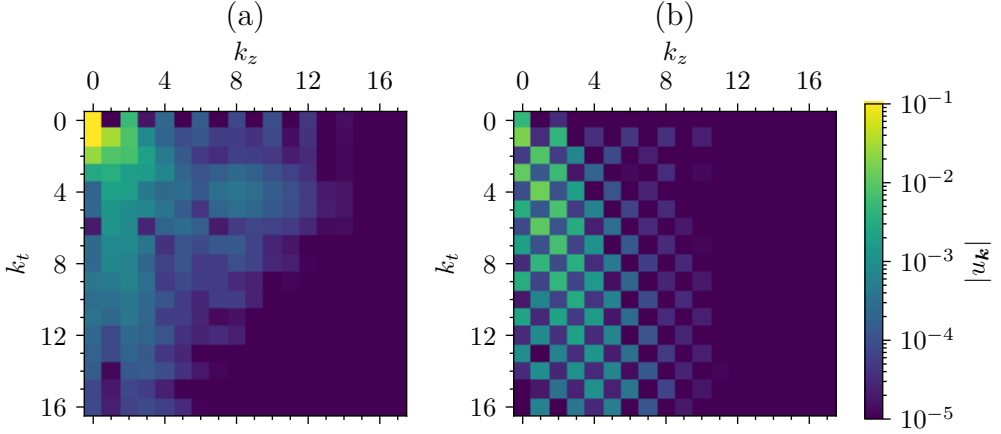


Figure 12: Spanwise and (positive) temporal power spectrum of the periodic solution in figure 11 at $y \approx -0.86$ in panel (a) and $y \approx 0$ in panel (b).

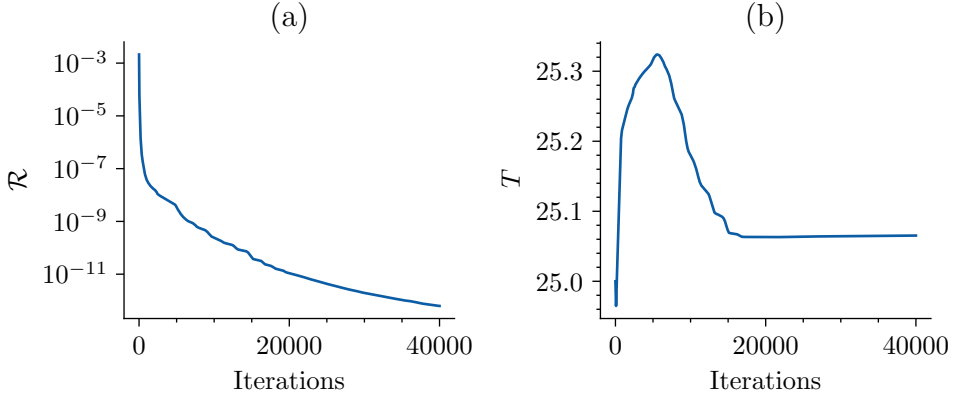


Figure 13: Traces of the global residual, panel (a), and the solution period, panel (b), of the periodic solution in figure 11 over the duration of the optimisation.

shows the spectrum of the periodic solution sampled at the two wall-normal positions $y \approx -0.86$ and $y \approx 0$. Each spectrum is a slice of the total spectrum such that only the positive temporal frequencies are shown, since the negative temporal frequencies are a reflection. An imbalance in the positive and negative temporal frequencies would manifest as travelling waves moving in the spanwise direction, which is not a feature of this solution. The general lack of spanwise motions in solutions to channel flows is a noted feature in Cvitanović & Gibson (2010). A checkerboard pattern is observed in the spectrum near the centreline of the flow, which represent the presence of the oscillating “tails” on either side of the vortices in figure 11. The most energetic mode is located at $(k_z, k_t) = (1, 0)$ which is mode that best fits the streamwise rolls that do not vary significantly with time. The spectrum at the location nearer the wall has a more continuous decay indicative of its less obvious spatial and temporal structure compared to the centre of the channel.

Figure 13 shows the trace of the global residual and period in panels (a) and (b), respectively. The final residual achieved is roughly $\mathcal{R} \approx 3 \times 10^{-13}$. The convergence rate of the problem is considerably slower after the initial rapid drop in residual than that observed in figure 8. This slow down can be explained by the increased degrees-of-freedom of the problem, both

in terms of the inclusion of an extra temporal dimension and in terms of the added resolution required at higher Reynolds numbers. The DNS typically takes on the order of thousands of time units to decay to the periodic flow implying a rather small leading Floquet exponent. The potential for very weak linear stability has the effect of slowing convergence rates, as will be discussed in more detail in section 6.

6. Conditioning of the Optimisation

The convergence rate of variational optimisation algorithms slows considerably near a minimum, a problem governed by the local curvature of the residual function (Nocedal & Wright 2006). The goal of this section is to link this conditioning directly to the underlying flow dynamics and to demonstrate that the resolvent modes provide a basis optimally constructed to improve the conditioning of the optimisation problem.

This curvature is characterized by the Hessian operator, which contains all second-derivative information at a point in optimisation space. The condition number of the Hessian measures the scale separation between the slowest and most rapid growth rates experienced by the objective when moving away from the minimum. A lower condition number implies improved convergence rates for gradient-based algorithms. A condition number of one signifies a perfectly quadratic local neighbourhood, while larger values indicate a long, narrow “valley”, which impedes convergence. It will be shown that the resolvent basis effectively minimizes this condition number.

The first step in the analysis is to derive a closed-form expression for the Hessian operator of the residual as defined in (2.6). To do this, first consider a minimum $\mathcal{R}[\mathbf{u}^*] = 0$, with \mathbf{u}^* denoting the flow field that solves the Navier-Stokes equations. Since \mathbf{u}^* is a minimum of (2.6) then we also know that $\delta\mathcal{R}/\delta\mathbf{u}^* = 0$. Assume that \mathbf{u}^* is an equilibrium. This does not change the content of the discussions that follow, only serving to simplify the mathematics by removing the need to use Floquet analysis. Adding an infinitesimal (potentially unsteady) perturbation to \mathbf{u}^* in the direction \mathbf{v} , where \mathbf{v} is incompressible and obeys a set of homogeneous boundary conditions similar to the local residual in (2.9), and expanding in terms of a Taylor series, only retaining the second-order term, leads to the following relation

$$\langle \mathbf{v}, \mathbf{H}\mathbf{v} \rangle_{\Omega_t} = \left\| \frac{\partial \mathbf{v}}{\partial t} - \mathbb{P} \mathcal{L}_{\mathbf{u}^*} \mathbf{v} \right\|_{\Omega_t}^2, \quad (6.1)$$

where \mathbf{H} denotes the Hessian operator, $\mathcal{L}_{\mathbf{u}^*}$ denotes the linearised Navier-Stokes operator evaluated at the minimum \mathbf{u}^* , and \mathbb{P} is the Leray projector as defined in section 3. The inclusion of the Leray projector is as a notational short-hand to avoid the added difficulty in having to explicitly account for the pressure gradient term in the Navier-Stokes equations. The detailed derivation of this equation is given in Appendix E. Let \mathbf{v} be a unimodal perturbation to that minimum, i.e. let $\mathbf{v} = \mathbf{v}_0 e^{i\omega t}$ for some arbitrary frequency where $\omega \in \mathbb{R}$ and some steady flow field \mathbf{v}_0 . This perturbation can be substituted into (6.1), effectively performing a Fourier transform, which gives

$$\langle \mathbf{v}_0, \mathbf{H}_\omega \mathbf{v}_0 \rangle_\Omega = \|(i\omega \mathbf{I} - \mathbb{P} \mathcal{L}_{\mathbf{u}^*}) \mathbf{v}_0\|_\Omega^2. \quad (6.2)$$

The Hessian operator is self-adjoint, as is apparent from (6.1), which means it is also normal. As such, the eigenvalues obey a strict ordering

$$0 = \mu_1 \leq \mu_2 \leq \dots \leq \mu_n \leq \dots, \quad (6.3)$$

and the condition number can be defined as $\kappa(\mathbf{H}_\omega) = \mu_N / \mu_1$, where μ_N is the largest

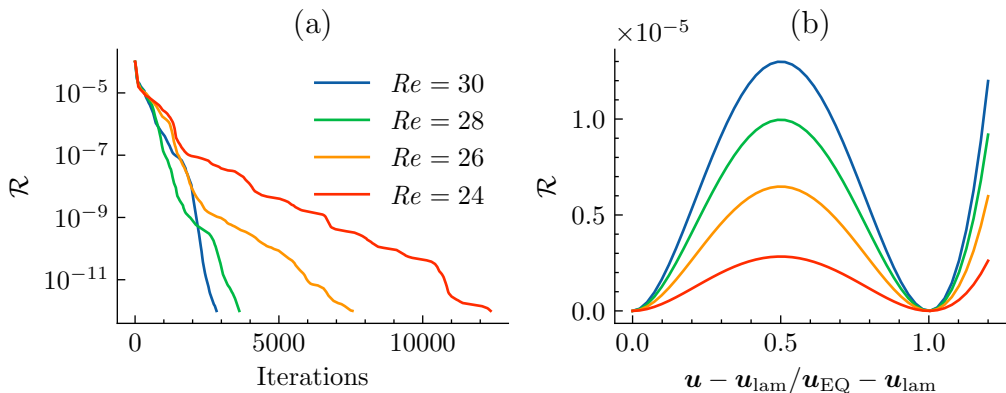


Figure 14: Residuals from optimisations of S1 at Reynolds numbers of $Re = 30, 28, 26, 24$. Panel (a) shows the residuals achieved during an optimisation of the equilibrium at each Reynolds number, and panel (b) shows the residual values between the final equilibrium solution and the laminar state. The residual resulting from a linear extrapolation away from the equilibrium in the same direction is also shown.

eigenvalue that can be resolved when the problem is discretised. The set of eigenvalues of \mathbf{H}_ω is unbounded since the eigenvalues of the Laplacian operator also unbounded.

It has been documented that the convergence rate of variational optimisers degrades near marginally stable solutions or bifurcation points (Farazmand 2016; Lakoba & Yang 2007). This phenomenon can be understood by considering the linear stability of the equilibrium solution \mathbf{u}^* , governed by the spectrum of $\mathcal{L}_{\mathbf{u}^*}$. Inspecting the derived expression for the Hessian in (6.2), it is clear that in the limit of any eigenvalue of $\mathcal{L}_{\mathbf{u}^*}$ approaching the imaginary axis (neutral stability), the action of the operator $i\omega\mathbf{I} - \mathcal{L}_{\mathbf{u}^*}$ becomes arbitrarily small near the frequency ω where that eigenvalue crosses. This implies that any perturbation \mathbf{v}_0 aligned with this marginally stable direction has a vanishingly small action from the Hessian, meaning the residual grows very slowly in this direction. In relation to the spectrum of \mathbf{H}_ω , this is equivalent to the smallest Hessian eigenvalue μ_1 approaching zero, which forces the condition number $\kappa(\mathbf{H}_\omega) \rightarrow \infty$. This mathematical insight is the basis for acceleration methods that assume the optimiser is traversing along the most marginally stable mode (Azimi *et al.* 2022; Ashtari & Schneider 2023), and several techniques have been devised to try and remove these problematic directions (Yang & Lakoba 2007), although they have not been applied to fluid dynamics problems.

This behaviour is demonstrated in figure 14, which shows the global residual over the course of a series of optimisation at different Reynolds numbers. As mentioned in section 4 at $Re \approx 20.7$ a bifurcation occurs where a new stable equilibrium solution is born out of the laminar state. Thus, as the Reynolds number gets closer to this bifurcation, the stable equilibrium gradually becomes more neutrally stable, leading to degrading convergence rates. The rate at which the convergence degrades as the Reynolds number approaches neutrality depends on the type of bifurcation that is occurring and how fast the particular eigenvalue that is switching stability approaches the imaginary axis.

The relationship in (6.2) can be rearranged to provide a closed-form expression for the Hessian operator

$$\mathbf{H}_\omega \mathbf{v}_0 = (i\omega\mathbf{I} - \mathbb{P}\mathcal{L}_{\mathbf{u}^*})^+ (i\omega\mathbf{I} - \mathbb{P}\mathcal{L}_{\mathbf{u}^*}) \mathbf{v}_0, \quad (6.4)$$

where $(\cdot)^+$ denotes the adjoint of an operator. Lifting the definition of the resolvent operator in (3.6) as $\mathbf{R}_\omega = (i\omega\mathbf{I} - \mathbb{P}\mathcal{L}_{\mathbf{u}^*})^{-1}\mathbb{P}$, the SVD defined in (3.7) can then be used to relate the

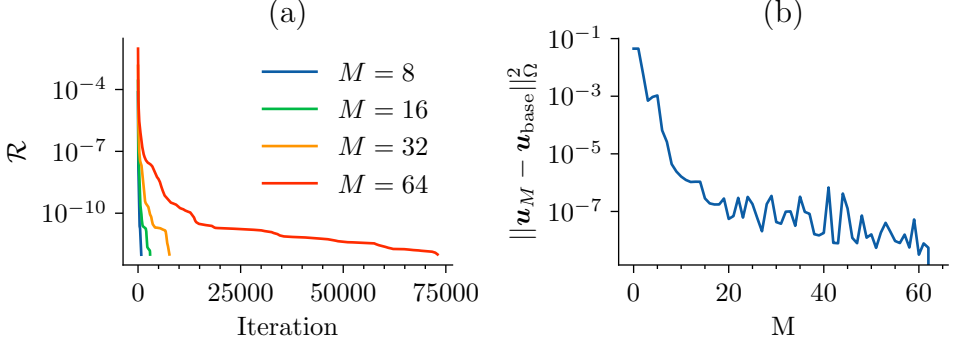


Figure 15: Panel (a): global residual traces for the optimisation of a perturbed S2 solution, performed using $M = 8, 16, 32$, and 64 resolvent modes, all starting from the same initial flow, using the L-BFGS algorithm. Panel (b): Accuracy of the resulting solutions found by the optimiser relative to the “base” case obtained for 64 resolvent modes, plotted against the number of modes used for the projection, each solution being converged such that $\mathcal{R} < 10^{-12}$.

non-normal growth mechanisms of \mathcal{L}_{u^*} to the spectrum of \mathbf{H}_ω

$$\mathbf{H}_\omega \mathbf{v}_0 = \sum_{i=1}^{\infty} \sigma_{\omega i}^{-2} \boldsymbol{\psi}_{\omega i} \langle \boldsymbol{\psi}_{\omega i}, \mathbf{v}_0 \rangle_{\Omega}. \quad (6.5)$$

Equation (6.5) represents an eigendecomposition of the Hessian, directly linking its spectrum to the resolvent of \mathcal{L}_{u^*} . The eigenvalues of \mathbf{H}_ω are the squared inverse of the resolvent’s singular values ($\mu_i = \sigma_{\omega i}^{-2}$), and their corresponding eigenmodes are identical to the resolvent response modes.

Therefore, the condition number $\kappa(\mathbf{H}_\omega)$ is primarily governed by the smallest retained singular value when the expansion is discretised. This relationship provides an optimal strategy for preconditioning since truncating the resolvent expansion to remove modes with the smallest singular values, one selectively eliminates the largest, most problematic eigenvalues from the Hessian. This optimally reduces the condition number, as it precisely targets and removes the directions associated with the strongest growth in the residual.

A key limitation is that these optimal resolvent modes depend on the linearised operator \mathcal{L}_{u^*} evaluated at the unknown minimum. Consequently, they cannot be used directly as the optimisation proceeds. The sensitivity of resolvent modes to the base flow remains poorly characterised, beyond the established dependence of singular values on the base flow (Brandt *et al.* 2011). We posit, however, that the higher-order modes exhibit universal structure, independent of the base flow, due to the dominance of viscous dissipation at small scales. This is favourable, as (6.5) indicates that rejecting these higher-order modes is the principal method for improving the Hessian’s condition number.

To demonstrate that rejecting higher order resolvent modes improves the convergence rate of the optimisation, we perform a series of optimisations starting from a perturbed state close to S3 from section 4 and 5.2 at $Re = 50$. The optimisation is performed using progressively fewer resolvent modes to generate the low-order model. The modes used are the same as those used in section 5.2, derived by linearising about the laminar base flow. The results of these optimisations are shown in figure 15.

Figure 15(a) shows the global residual traces for the perturbed field using 8, 16, 32, and 64 resolvent modes. All the residuals reduce at a high rate initially, indicating the power of the variational optimiser to quickly seek out the solution primarily by modifying the

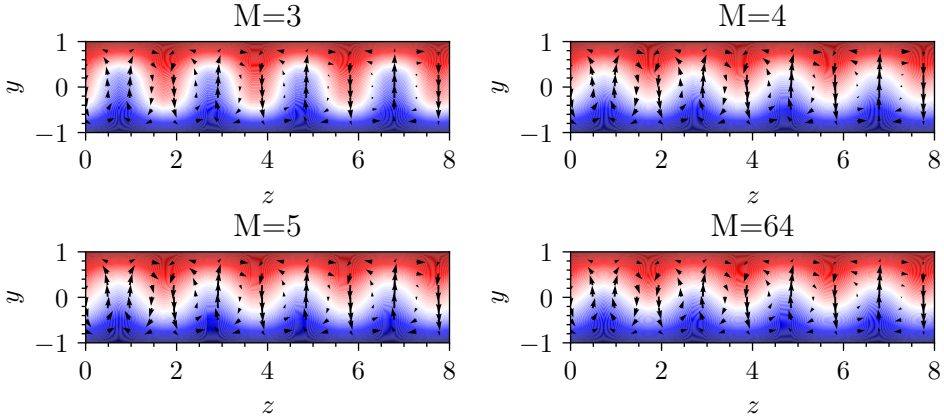


Figure 16: Snapshots of the solutions obtained from the projected optimisation of the perturbed S3 solution.

large-scale structures. This initially fast decrease, however, eventually gives way to a slower convergence rate, as is typically observed in the literature (Azimi *et al.* 2022; Ashtari & Schneider 2023). The primary point to note from figure 15(a) is that both the degree of the eventual slowdown in convergence rate and the iteration count at which it occurs are strongly linked to the number of modes used for the Galerkin projection. The smaller the number of modes used the faster the overall convergence rate is, achieving the minimum residual in orders of magnitude fewer iterations than when more modes are retained. Specifically, the case of $M = 64$ resolvent modes achieved its final residual after roughly 10^5 iterations, whereas the $M = 8$ case shows the same residual after only hundreds of iterations. The figure clearly demonstrates the truncation of the resolvent modes, derived about the laminar base flow, associated with the smallest singular values improves convergence. This provides confirmation that the condition number of the Hessian at the minimum is improved, even though the resolvent modes are derived relative to a different base flow. A final note is that an immediate result of truncating the resolvent modes is to reduce the global residual of the initial field. This is a result of the noise introduced in the perturbation of S3 being truncated in the projection, reducing the smaller scale noise present in the starting flow.

In addition to the convergence rates, figure 15(b) shows the accuracy of the resulting solutions obtained from the projected optimisations plotted against the number of modes used for the Galerkin projection. The accuracy was computed as the norm of the difference between the field obtained from the projected optimisation, denoted with \mathbf{u}_M , and a base solution, denoted with \mathbf{u}_{base} , which was taken as the solution obtained using the full set of resolvent modes, i.e. $M = 64$. As the number of modes used for the projection is increased, the error between the obtained solution and the base decreases, initially quite quickly when the number of modes used is small, but then reducing slower and saturating at around $\|\mathbf{u}_M - \mathbf{u}_{\text{base}}\|_{\Omega_t}^2 \approx 10^{-7}$ at roughly $M = 20$. The initial decrease in the error is a result of the extra modes being added having a relatively large contribution to the solution S3, with the observed exponential decrease in error typical of spectral methods. The saturation of the solution error as more modes are added is due to tolerances associated with the small changes in the minimum position and initial starting point for the optimisation for each value M .

Figure 16 demonstrates that even a small number of resolvent modes can faithfully reconstruct the large-scale structure of a solution, despite potentially poor quantitative accuracy. It shows snapshots of the solutions obtained using $M = 3$, $M = 4$, $M = 5$,

and the base case $M = 64$. Each solution displays the desired streamwise rolls with the correct spanwise wavelength. The solution for $M = 3$ has noticeable qualitative differences from the base solution, consistent with its $\mathcal{O}(1)$ error in figure 15(b). However, the solutions for $M = 4$ and $M = 5$ are far more similar to the base solution visually, even though their quantitative error remains significant.

Taking these results together, we conclude that retaining a sufficiently small number of modes allows the projected optimisation to reconstruct the dominant structures of the desired solution, albeit at the cost of final accuracy, but with a significantly improved convergence rate. This presents a practical trade-off. If only the large-scale structures are sought, aggressively truncating the number of modes yields a solution far more rapidly. This could be used to initialise searches for ECS, using a truncated set of modes to quickly reduce the residual and capture the large-scale flow. The number of modes could then be increased to resolve smaller scales, or the output could be handed off to a Newton-GMRES-hookstep method for final convergence, akin to the approach in Farazmand (2016).

7. Conclusions

This work makes two primary contributions to the variational optimisation of exact coherent structures. First, we introduce a methodology for treating wall-bounded periodic flows by projecting the optimisation onto a basis of divergence-free resolvent modes that inherently enforce no-slip boundary conditions and incompressibility. This approach, which extends the methods of Farazmand (2016) and Azimi *et al.* (2022), directly embeds the required constraints, alleviating a key theoretical difficulty. This is in contrast to the approach taken in Ashtari & Schneider (2023) using the influence matrix method. In doing so, it unifies the optimisation framework with the resolvent-based modelling framework of McKeon & Sharma (2010), providing a direct method to “close the loop” in resolvent analysis (Barthel *et al.* 2021) by solving for the self-consistent, finite-amplitude velocity field that sustains the chosen forcing modes. Second, we establish a formal link between the conditioning of the optimisation problem and resolvent analysis via the Hessian operator. We demonstrate that truncating the resolvent basis not only creates a reduced-order model but also acts as an effective preconditioner thereby significantly accelerating convergence.

The projected optimisation methodology is applied to 2-dimensional, 3-component rotating plane Couette flow, with all analysis performed with a rotation number of $Ro = 0.5$. Both equilibria and periodic solutions are sought in this work. The optimiser successfully identified equilibria that are not observed in DNS at $Re = 50$ from various initial conditions. At $Re = 400$, a stable periodic solution was obtained by initialising the optimiser with a perturbed DNS solution. In this case the residual decreased from $\mathcal{R} > 10^{-3}$ to $\mathcal{R} < 10^{-12}$ in roughly 40,000 iterations, over half of which occurred in the first 5,000. The slower convergence for the optimisation of the periodic solution is argued to be primarily a result of the increase in the degrees-of-freedom of the system and the possible weak linear stability of the solution.

We also investigated the factors that affect the asymptotic convergence rate of the optimisation via the conditioning of the Hessian operator at a global minimum. It is shown that the closer a solution is to being marginally stable the larger the condition number and thus the slower the convergence, a behaviour which has been discussed in Farazmand (2016). In addition, a direct link is established between the condition number of the Hessian and the resolvent expansion at a global minimum. It is shown that truncating the resolvent expansion by excluding the smallest singular values is equivalent to removing the fastest growing directions in the residual which optimally reduces the condition number of the Hessian operator. The improved convergence is demonstrated by optimising to an equilibrium solution

using a reduced number of resolvent modes. Physically, this equivalence arises because the the Laplace operator dominates the higher-order behaviour of the Hessian eigenmodes and the resolvent modes regardless of the base flow around which the linearisations is performed. This operator is primarily responsible for the degradation in convergence rates, owing to its rapid dissipation of high-frequency components, particularly at higher Reynolds numbers where small-scale motions must be resolved. Removing the highest order resolvent modes is equivalent to removing these modes of growth from the optimisation. The resulting reduced-order solutions obtained from the optimisation on a truncated set of modes were shown to closely approximate the original solution derived from the full basis set. Specifically only a handful of modes were shown to be very close to the original solution. This means that even though the solution obtained using a very reduced set of modes does not accurately reconstruct the true solution in state-space, it could be used to initialise a more accurate search with superior convergence properties such as the Newton-GMRES-hookstep method.

Ultimately, the Galerkin projection not only enables the construction of solutions for general wall-bounded flows but also enhances the capability of variational optimisation. Coupled with its robustness to initial conditions, the improved convergence makes the method more practical both as a stand-alone solver and as a preconditioning step for root-finding approaches. The ability to truncate the modal basis further extends applicability to larger problems than are typically tractable with global solvers.

The projected variational optimiser presented in this work has two primary limitations. The most immediate is its high memory requirement for storing the high-dimensional state vector, which can become prohibitive for extending this method to fully three-dimensional turbulent flows. A promising path to mitigate this is leveraging parallel computing architectures, for which this framework is exceptionally well-suited since unlike traditional DNS the optimisation can be parallelised in the temporal dimension in addition to the spatial ones. A highly parallel implementation of the methodology would also permit an investigation into so-called “quasi-trajectories” from Burton *et al.* (2025) for turbulent flows. The second, more fundamental limitation is the efficacy of the resolvent basis being intrinsically linked to the chosen base flow. Determining a general principle for selecting the most effective base flow to yield useful, dynamically relevant modes requires extra investigation and represents a crucial direction for future work.

Appendix A. Residual Gradient Derivation

A.1. Velocity Field Derivative

Before beginning the derivation, we shall define a modified optimisation problem that enforces the incompressibility constraint through a Lagrange multiplier

$$\min_{\mathbf{u} \in \mathcal{P}_{\text{BC}, T}} \mathcal{R}[\mathbf{u}, q] = \frac{1}{2} \|\mathbf{r}\|_{\Omega_t}^2 + \langle q, \nabla \cdot \mathbf{u} \rangle_{\Omega_t}, \quad (\text{A } 1)$$

where

$$\mathcal{P}_{T, \text{BC}} = \left\{ \mathbf{u} \in \chi \mid \mathbf{u}|_{t=0} = \mathbf{u}|_{t=T}, \mathbf{u}|_{y=\pm 1} = \mathbf{u}_w, \mathbf{u} \text{ obeys periodic BCs} \right\}, \quad (\text{A } 2)$$

is the space of velocity fields that obey the boundary conditions, but aren't necessarily incompressible. Also define the space of fields that obey the homogeneous boundary conditions

$$\mathcal{P}_{T, \text{HBC}} = \left\{ \mathbf{u} \in \chi \mid \mathbf{u}|_{t=0} = \mathbf{u}|_{t=T}, \mathbf{u}|_{y=\pm 1} = 0, \mathbf{u} \text{ obeys periodic BCs} \right\}, \quad (\text{A } 3)$$

which will be useful for the later parts of this derivation. To derive the gradient first define a perturbation to the velocity field $\mathbf{u} \rightarrow \mathbf{u} + \epsilon \mathbf{v}$ where $0 < \epsilon \in \mathbb{R}$ is small enough such that $\epsilon^2 \approx 0$. The perturbation is incompressible and obeys the homogeneous boundary conditions, i.e. $\mathbf{v} \in \mathcal{P}_{T,\text{HBC}}$ and $\nabla \cdot \mathbf{v} = 0$. Calculus of variations provides the following identity

$$\left[\frac{d}{d\epsilon} \mathcal{R} [\mathbf{u} + \epsilon \mathbf{v}] \right]_{\epsilon=0} = \left\langle \frac{\delta \mathcal{R}}{\delta \mathbf{u}}, \mathbf{v} \right\rangle_{\Omega_t}. \quad (\text{A } 4)$$

To derive the expression for $\delta \mathcal{R} / \delta \mathbf{u}$ it is required to propagate the perturbation \mathbf{v} through all the variables that depend on \mathbf{u} . The local residual perturbation is

$$\mathbf{r} (\mathbf{u} + \epsilon \mathbf{v}) = \mathbf{r} + \delta \mathbf{r} = \frac{\partial \mathbf{u}}{\partial t} + \epsilon \frac{\partial \mathbf{v}}{\partial t} - \mathcal{N} (\mathbf{u}) - \delta \mathcal{N} - \nabla p - \epsilon \nabla \delta p,$$

where

$$\mathcal{N} (\mathbf{u}) = - (\mathbf{u} \cdot \nabla) \mathbf{u} + \frac{1}{Re} \Delta \mathbf{u}. \quad (\text{A } 5)$$

Rearranging for $\delta \mathbf{r}$ gives

$$\delta \mathbf{r} = \epsilon \left(\frac{\partial \mathbf{v}}{\partial t} - \nabla \delta p \right) - \delta \mathcal{N}. \quad (\text{A } 6)$$

The perturbation term $\delta \mathcal{N}$ can be computed as

$$\begin{aligned} \mathcal{N} (\mathbf{u} + \epsilon \mathbf{v}) &= \mathcal{N} + \delta \mathcal{N} \\ &= - ((\mathbf{u} + \epsilon \mathbf{v}) \cdot \nabla) (\mathbf{u} + \epsilon \mathbf{v}) + \frac{1}{Re} \Delta (\mathbf{u} + \epsilon \mathbf{v}) \\ &= - (\mathbf{u} \cdot \nabla) \mathbf{u} + \frac{1}{Re} \Delta \mathbf{u} - \epsilon \left(- (\mathbf{u} \cdot \nabla) \mathbf{v} - (\mathbf{v} \cdot \nabla) \mathbf{u} + \frac{1}{Re} \Delta \mathbf{v} \right) + O(\epsilon^2), \end{aligned}$$

which when rearranged for $\delta \mathcal{N}$, and neglecting the ϵ^2 term, gives

$$\delta \mathcal{N} = \epsilon \left(- (\mathbf{u} \cdot \nabla) \mathbf{v} - (\mathbf{v} \cdot \nabla) \mathbf{u} + \frac{1}{Re} \Delta \mathbf{v} \right) + O(\epsilon^2). \quad (\text{A } 7)$$

The perturbation in the global residual defined in (A 1), called the first variation in \mathcal{R} , is given by

$$\begin{aligned} \mathcal{R} [\mathbf{u} + \epsilon \mathbf{v}] &= \frac{1}{2} \|\mathbf{r} + \delta \mathbf{r}\|_{\Omega_t}^2 + \langle q, \nabla \cdot (\mathbf{u} + \epsilon \mathbf{v}) \rangle_{\Omega_t} \\ &= \frac{1}{2} \|\mathbf{r}\|_{\Omega_t}^2 + \langle \mathbf{r}, \delta \mathbf{r} \rangle_{\Omega_t} + \langle \delta \mathbf{r}, \delta \mathbf{r} \rangle_{\Omega_t} + \langle q, \nabla \cdot \mathbf{u} \rangle_{\Omega_t} + \epsilon \langle q, \nabla \cdot \mathbf{v} \rangle_{\Omega_t}. \end{aligned}$$

Substituting (A 6) and (A 7) into the expression above, neglecting all the ϵ^2 terms, gives

$$\begin{aligned} \mathcal{R} [\mathbf{u} + \epsilon \mathbf{v}] &= \frac{1}{2} \|\mathbf{r}\|_{\Omega_t}^2 + \langle q, \nabla \cdot \mathbf{u} \rangle_{\Omega_t} \\ &+ \epsilon \left(\left\langle \mathbf{r}, \frac{\partial \mathbf{v}}{\partial t} - (\mathbf{u} \cdot \nabla) \mathbf{v} - (\mathbf{v} \cdot \nabla) \mathbf{u} + \frac{1}{Re} \Delta \mathbf{v} - \nabla \delta p \right\rangle_{\Omega_t} + \langle q, \nabla \cdot \mathbf{v} \rangle_{\Omega_t} \right) + O(\epsilon^2). \end{aligned} \quad (\text{A } 8)$$

Then, substituting (A 8) into (A 4) provides a relationship for the functional derivative

$$\left\langle \frac{\delta \mathcal{R}}{\delta \mathbf{u}}, \mathbf{v} \right\rangle_{\Omega_t} = \left\langle \mathbf{r}, \frac{\partial \mathbf{v}}{\partial t} - (\mathbf{u} \cdot \nabla) \mathbf{v} - (\mathbf{v} \cdot \nabla) \mathbf{u} + \frac{1}{Re} \Delta \mathbf{v} - \nabla \delta p \right\rangle_{\Omega_t} + \langle q, \nabla \cdot \mathbf{v} \rangle_{\Omega_t}. \quad (\text{A } 9)$$

To obtain a closed-form expression for $\delta\mathcal{R}/\delta\mathbf{u}$ it is necessary to derive the adjoint of all the operators on the right-hand side of (A 9) such that it resembles the left-hand side. Starting with the time derivative

$$\left\langle \mathbf{r}, \frac{\partial \mathbf{v}}{\partial t} \right\rangle_{\Omega_t} = \left\langle -\frac{\partial \mathbf{r}}{\partial t}, \mathbf{v} \right\rangle_{\Omega_t}, \quad (\text{A } 10)$$

where integration by parts has been used, with the boundary terms (at $t = 0$ and $t = T$) cancel due to the flow being periodic in time. To simplify the derivation, we will make use of the product rule for divergence

$$\nabla \cdot (\mathbf{u}\mathbf{v}) = \mathbf{u}\nabla \cdot \mathbf{v} + \mathbf{v} \cdot \nabla \mathbf{u}, \quad (\text{A } 11)$$

as well as the divergence theorem

$$\int_{\Omega} \nabla \cdot \mathbf{u} \, dV = \int_{\partial\Omega} \mathbf{u} \cdot \hat{\mathbf{n}} \, dS, \quad (\text{A } 12)$$

where $\hat{\mathbf{n}}$ is an outwardly pointing normal vector on the surface $\partial\Omega$, and dV and dS are infinitesimal volume and surface elements, respectively. Note that for any field $\mathbf{u} \in \mathcal{P}_{\text{HBC}}$ the surface integral vanishes, i.e.

$$\int_{\partial\Omega} \mathbf{u} \cdot \hat{\mathbf{n}} \, dS = 0, \quad (\text{A } 13)$$

due to all the periodic boundary terms cancelling, and the homogeneous no-slip boundary terms being equal to zero. Thus, using (A 11) and (A 12), for the first of the convective terms we have

$$\langle \mathbf{r}, (\mathbf{u} \cdot \nabla) \mathbf{v} \rangle_{\Omega_t} = \int_0^T \left(\int_{\partial\Omega} (\mathbf{r} \cdot \mathbf{v}) \mathbf{u} \cdot \hat{\mathbf{n}} \, dS - \int_{\Omega} ((\mathbf{u} \cdot \nabla) \mathbf{r}) \cdot \mathbf{v} \, dV \right) dt. \quad (\text{A } 14)$$

Using the fact that $\mathbf{v} \in \mathcal{P}_{\text{HBC}}$ and $\mathbf{u} \in \mathcal{P}_{\text{BC}}$, the surface integral vanish, leaving the following

$$\langle \mathbf{r}, (\mathbf{u} \cdot \nabla) \mathbf{v} \rangle_{\Omega_t} = \langle -(\mathbf{u} \cdot \nabla) \mathbf{r}, \mathbf{v} \rangle_{\Omega_t}. \quad (\text{A } 15)$$

The second convective term is slightly simpler due to \mathbf{v} not appearing in any derivatives

$$\langle \mathbf{r}, (\mathbf{v} \cdot \nabla) \mathbf{u} \rangle_{\Omega_t} = \langle \mathbf{r}, (\nabla \mathbf{u}) \mathbf{v} \rangle_{\Omega_t} = \langle (\nabla \mathbf{u})^\top \mathbf{r}, \mathbf{v} \rangle_{\Omega_t}, \quad (\text{A } 16)$$

where $\nabla \mathbf{u}$ is the gradient of the vector field \mathbf{u} . In Cartesian coordinates this looks like the gradient of the scalar components on \mathbf{u} stacked on top of each other to form a matrix. Next, the diffusion term

$$\langle \mathbf{r}, \Delta \mathbf{v} \rangle_{\Omega_t} = \int_0^T \left(\int_{\partial\Omega} (\mathbf{r} \cdot \nabla \mathbf{v} - \nabla \mathbf{r} \cdot \mathbf{v}) \cdot \hat{\mathbf{n}} \, dS + \int_{\Omega} \Delta \mathbf{r} \cdot \mathbf{v} \, dV \right) dt, \quad (\text{A } 17)$$

where the product rule and divergence theorem have been used twice to effectively integrate by parts the second-order derivatives in the Laplacian. The second of the boundary integrals vanish due to $\mathbf{v} \in \mathcal{P}_{T,\text{HMB}}$, however, the other boundary integral does not by default since we have not imposed any extra restrictions on the gradients of \mathbf{v} . To resolve this, it is necessary to impose the $\mathbf{r} \in \mathcal{P}_{T,\text{HBC}}$, enforcing that \mathbf{r} vanishes at the walls, which means the first boundary integral also vanishes, giving

$$\langle \mathbf{r}, \Delta \mathbf{v} \rangle_{\Omega_t} = \langle \Delta \mathbf{r}, \mathbf{v} \rangle_{\Omega_t}. \quad (\text{A } 18)$$

Moving to the pressure gradient we have

$$\langle \mathbf{r}, \nabla \delta p \rangle_{\Omega_t} = \int_0^T \left(\int_{\partial\Omega} \delta p (\mathbf{r} \cdot \hat{\mathbf{n}}) \, dS - \int_{\Omega} (\nabla \cdot \mathbf{r}) \delta p \, dV \right) dt. \quad (\text{A } 19)$$

Since we know that $\mathbf{r} \in \mathcal{P}_{T,\text{HBC}}$ as prescribed by the adjoint of the diffusion term, the boundary term here must vanish, leaving

$$\langle \mathbf{r}, \nabla \delta p \rangle_{\Omega_t} = \langle -\nabla \cdot \mathbf{r}, \delta p \rangle_{\Omega_t}. \quad (\text{A } 20)$$

The divergence of the residual is actually the PPE, and since the pressure field is assumed to satisfy this equation we also know that $\nabla \cdot \mathbf{r} = 0$, and thus (A 20) is also zero. This just leaves the divergence term for the Lagrange multiplier, enforcing the divergence-free evolution of the velocity field \mathbf{u} under the optimisation problem given in (A 1). Due to the symmetry of the inner-product (in the case of real fields), it is easy to see that the adjoint of the divergence operator is the negative gradient operator. Applying this result gives

$$\langle q, \nabla \cdot \mathbf{v} \rangle_{\Omega_t} = \int_0^T \int_{\Omega} -\nabla q \cdot \mathbf{v} dV dt = \langle -\nabla q, \mathbf{v} \rangle_{\Omega_t}. \quad (\text{A } 21)$$

Combining all of these results and substituting them into the right-hand side of (A 9) provides

$$\left\langle \frac{\delta \mathcal{R}}{\delta \mathbf{u}}, \mathbf{v} \right\rangle_{\Omega_t} = \left\langle -\frac{\partial \mathbf{r}}{\partial t} - (\mathbf{u} \cdot \nabla) \mathbf{r} + (\nabla \mathbf{u})^\top - \frac{1}{Re} \Delta \mathbf{r} - \nabla q, \mathbf{v} \right\rangle_{\Omega_t}, \quad (\text{A } 22)$$

which provides the desired closed-form expression for the functional derivative of \mathcal{R} with respect to \mathbf{u}

$$\frac{\delta \mathcal{R}}{\delta \mathbf{u}} = -\frac{\partial \mathbf{r}}{\partial t} - (\mathbf{u} \cdot \nabla) \mathbf{r} + (\nabla \mathbf{u})^\top - \frac{1}{Re} \Delta \mathbf{r} - \nabla q, \quad (\text{A } 23)$$

with the additional constraints $\mathbf{r} \in \mathcal{P}_{\text{HBC}}$ and $\nabla \cdot \mathbf{r}$. The boundary constraints on \mathbf{r} at the boundaries is an instance of a natural boundary conditions, and are necessary to enforce. If they are not strictly enforced, then the residual gradient given in (A 23) is not guaranteed to be a descent direction. A similar interpretation applies to $\nabla \cdot \mathbf{r} = 0$ except it applies throughout the whole domain rather than just the boundaries.

A.2. Fundamental Frequency Derivative

The derivative of \mathcal{R} with respect to the fundamental frequency ω is simpler to derive due to it not being functional and requiring methods from variational calculus. First, define a new scaled time $t' = \omega t$ which then leads to a the following relationship between the time derivatives $\partial/\partial t = \omega \partial/\partial t'$. Using this scaled time in the definition of the local residual in (2.5), and then substitute the resulting expression into the definition of the global residual

$$\begin{aligned} \mathcal{R} = \frac{\omega^2}{2} \left\| \frac{\partial \mathbf{u}}{\partial t'} \right\|_{\Omega_t}^2 - \omega \left\langle \frac{\partial \mathbf{u}}{\partial t'}, -(\mathbf{u} \cdot \nabla) \mathbf{u} + \frac{1}{Re} \mathbf{v} - \nabla p \right\rangle_{\Omega_t} \\ + \frac{1}{2} \left\| -(\mathbf{u} \cdot \nabla) \mathbf{u} + \frac{1}{Re} \mathbf{v} - \nabla p \right\|_{\Omega_t}^2. \end{aligned} \quad (\text{A } 24)$$

Fixing the particular velocity field \mathbf{u} under consideration makes this a quadratic function, with a single global minimum at some ω^* . This global minimum could be derived rather simply, however using it directly during the optimisation was found to lead to very erratic behaviour, especially when far away from a solution. Taking the derivative of (A 24) with respect to ω gives

$$\frac{\partial \mathcal{R}}{\partial \omega} = \omega \left\| \frac{\partial \mathbf{u}}{\partial t'} \right\|_{\Omega_t}^2 - \left\langle \frac{\partial \mathbf{u}}{\partial t'}, -(\mathbf{u} \cdot \nabla) \mathbf{u} + \frac{1}{Re} \mathbf{v} - \nabla p \right\rangle_{\Omega_t}. \quad (\text{A } 25)$$

With a slight rearrangement the following simplified expression is obtained

$$\frac{\partial \mathcal{R}}{\partial \omega} = \frac{1}{\omega} \left\langle \frac{\partial \mathbf{u}}{\partial t}, \mathbf{r} \right\rangle_{\Omega_t}. \quad (\text{A } 26)$$

A similar expression can be obtained for the derivative with respect to the solution period $T = 2\pi/\omega$ using the chain rule

$$\frac{\partial \mathcal{R}}{\partial T} = -\frac{1}{T} \left\langle \frac{\partial \mathbf{u}}{\partial t}, \mathbf{r} \right\rangle_{\Omega_t}. \quad (\text{A } 27)$$

Appendix B. DAE Form of Variational Optimisation

In the literature (Farazmand 2016; Azimi *et al.* 2022; Ashtari & Schneider 2023) the variational optimisation is derived using an adjoint variational dynamics formulation. Using the same notation, where τ represents the fictitious time introduced to parametrise the evolution of the variational dynamics, we can say that

$$\frac{\partial \mathbf{u}}{\partial \tau} := -\frac{\delta \mathcal{R}}{\delta \mathbf{u}}, \quad \frac{d\omega}{d\tau} := -\frac{\partial \mathcal{R}}{\partial \omega}, \quad (\text{B } 1)$$

Using this definition the gradient-based optimisation problem can be restated in the form of a Differential-Algebraic Equation (DAE) for the evolution of the spatio-temporal flow field

$$\frac{\partial \mathbf{u}}{\partial \tau} = \frac{\partial \mathbf{r}}{\partial t} + (\mathbf{u} \cdot \nabla) \mathbf{r} - (\nabla \mathbf{u})^\top \mathbf{r} + \frac{1}{Re} \Delta \mathbf{r} - \nabla q, \quad (\text{B } 2a)$$

$$\frac{\partial \omega}{\partial \tau} = -\frac{1}{\omega} \left\langle \frac{\partial \mathbf{u}}{\partial t}, \mathbf{r} \right\rangle_{\Omega_t}, \quad (\text{B } 2b)$$

$$0 = \frac{\partial \mathbf{u}}{\partial t} + \nabla p + (\mathbf{u} \cdot \nabla) \mathbf{u} - \frac{1}{Re} \Delta \mathbf{u} - \mathbf{r}, \quad (\text{B } 2c)$$

$$0 = \nabla \cdot \mathbf{u}, \quad (\text{B } 2d)$$

$$0 = \nabla \cdot \mathbf{r}, \quad (\text{B } 2e)$$

$$0 = \mathbf{u}|_{y=\pm 1} - \mathbf{u}_w, \quad (\text{B } 2f)$$

$$0 = \mathbf{r}|_{y=\pm 1}, \quad (\text{B } 2g)$$

$$(\text{B } 2h)$$

In the work of Azimi *et al.* (2022); Ashtari & Schneider (2023), equation (B 2) is solved using a simple first-order Euler scheme to explicitly step forward the solution by $\Delta\tau$. The use of the Euler method was justified as the accuracy of the intermediate result does not matter, just the accuracy of the solution at the end once \mathcal{R} becomes sufficiently small. This allowed for larger step sizes in τ . Farazmand (2016) uses a Runge-Kutta time stepping method in τ to improve accuracy, but this still suffers from the same slow convergence expected from gradient descent methods. However, as shown here, the problem can be viewed simply as an optimisation problem, where the goal is to minimise \mathcal{R} as much as possible regardless of the route taken in the loop space to do so. This means the intermediate accuracy of any time-stepping scheme in $\Delta\tau$ is not productive. Instead, more broad optimisation algorithms can be used, that trade the exact evolution prescribed by (B 2a) and (B 2b) for convergence to smaller residuals in far fewer iterations. This is displayed in section 5.2 where gradient descent (mathematically equivalent to the Euler method in τ) is compared with common quasi-Newton optimisation algorithms.

Appendix C. Resolvent for 2D3C RPCF

In this work we use resolvent analysis to generate an divergence-free and no-slip orthonormal basis set for the velocity and local residual fields. The exact form of the operators defined in section 3 for 2D3C RPCF is given here. First, the (nonlinear) Navier-Stokes operator is defined as

$$\mathcal{N}(\mathbf{u}_b) = -(\mathbf{u}_b \cdot \nabla) \mathbf{u}_b + \frac{1}{Re} \Delta \mathbf{u}_b - Ro (\hat{\mathbf{k}} \times \mathbf{u}_b), \quad (\text{C } 1)$$

where the base pressure field p_b is not included since it is projected away by the Leray projector \mathbb{P} in (3.2). The linearised Navier-Stokes operator evaluated at the base flow \mathbf{u}_b , $\mathcal{L}_{\mathbf{u}_b}$, is given by

$$\mathcal{L}_{\mathbf{u}_b} \mathbf{u}' = -(\mathbf{u}_b \cdot \nabla) \mathbf{u}' - (\nabla \mathbf{u}_b) \mathbf{u}' + \frac{1}{Re} \Delta \mathbf{u}' - Ro \hat{\mathbf{k}} \times \mathbf{u}'. \quad (\text{C } 2)$$

where again the pressure is not included due to the Leray projector in (3.2). Assuming $\mathbf{u}_b = u_b(y)\hat{\mathbf{i}}$, and using the definition of the resolvent in section 3, the final expression for the operator for 2D3C RPCF is expressed as

$$\mathbf{R}_k = \begin{pmatrix} ik_t \omega - \frac{1}{Re} \Delta_k & \frac{\partial u_b}{\partial y} - Ro & 0 \\ Ro & ik_t \omega - \frac{1}{Re} \Delta_k & 0 \\ 0 & 0 & ik_t \omega - \frac{1}{Re} \Delta_k \end{pmatrix}^{-1} \mathbb{P}. \quad (\text{C } 3)$$

where $\Delta_k = \partial^2 / \partial y^2 - (\beta k_z)^2$.

Appendix D. DNS Numerical Methods

The velocity vector field is conveniently decomposed into the laminar base state, and the velocity fluctuation denoted in this appendix as $\mathbf{u}(y, z, t) = (u \ v \ w)^\top$. A formulation using the streamwise component of the vorticity perturbation $\omega_x = \partial w / \partial y - \partial v / \partial z$, and the streamwise (fluctuation) velocity u , is used to numerically solve the problem (4.1). This formulation is used to eliminate complications arising from the pressure term. Because the domain is two-dimensional the stream function ψ , related to the transverse and wall-normal (fluctuation) velocity components by the relations $w = -\partial \psi / \partial y$ and $v = \partial \psi / \partial z$, and to the vorticity by the Poisson-type equation $\Delta \psi = -\omega$, is introduced. Introduction of the streamfunction ensure that the continuity equation is satisfied. With these definitions, the coupled system of nonlinear Partial Differential Equations (PDEs)

$$\frac{\partial u}{\partial t} = -\frac{\partial \psi}{\partial z} \frac{\partial u}{\partial y} + \frac{\partial \psi}{\partial y} \frac{\partial u}{\partial z} + \frac{\partial \psi}{\partial z} (Ro - 1) + \frac{1}{Re} \Delta u, \quad (\text{D } 1a)$$

$$\frac{\partial \omega}{\partial t} = -\frac{\partial \psi}{\partial z} \frac{\partial \omega}{\partial y} + \frac{\partial \psi}{\partial y} \frac{\partial \omega}{\partial z} - \frac{\partial u}{\partial z} Ro + \frac{1}{Re} \Delta \omega, \quad (\text{D } 1b)$$

governs the evolution of the streamwise (fluctuation) velocity and vorticity. A spectral spatial discretisation of (D 1) is adopted along the axial direction by introducing the truncated Fourier expansion

$$f(z, y, t) = \sum_{k=-N/2}^{N/2-1} f_k(y, t) \exp(ik_z \beta z) \quad (\text{D } 2)$$

for u , ω and ψ , with $\beta = 2\pi/L_z$, and with k_z being the spanwise wavenumber. Projection of the governing equations (D 1) onto (D 2) leads to a system of sets of three one-dimensional coupled partial differential equations in the wall-normal direction y , for each wave number k_z . This system of PDEs is then discretised in time using a fairly standard splitting approach. The viscous term is treated implicitly using a Crank-Nicholson method, while the nonlinear term and the term arising from the rotation and the mean flow shear are integrated explicitly via a second-order accurate Adams-Bashforth method. The nonlinear term is treated pseudo-spectrally, see Canuto *et al.* (1988), whereas de-aliasing was not found necessary, given the low resolution requirements. Temporal discretisation results in a system of ordinary differential equations in the space variable y , having the form of Helmholtz problems for each wave number k_z and for the three flow variables. These are solved at each time step using a second-order centred finite difference scheme, leading to sparse banded system solved directly by a Gaussian elimination method with pivoting.

Appendix E. Hessian Operator Derivation

To derive the Hessian operator, first take the definition of the local residual in (2.5) and project it onto the divergence-free subspace using the Leray projector as defined in section 3

$$\mathbf{r} = \frac{\partial \mathbf{u}}{\partial t} - \mathbb{P}\mathcal{N}(\mathbf{u}), \quad (\text{E } 1)$$

where the local residual itself is unaffected by the projection since it is divergence-free by construction. Consider a solution to the optimisation problem denoted as \mathbf{u}^* . A perturbation to the solution \mathbf{u}^* by some arbitrary velocity field \mathbf{v} that is incompressible and obeys the appropriate boundary conditions is applied. The global residual \mathcal{R} can then be expanded at the minimum using a Taylor series

$$\mathcal{R}[\mathbf{u}^* + \epsilon \mathbf{v}] = \mathcal{R}[\mathbf{u}^*] + \epsilon \left\langle \frac{\delta \mathcal{R}}{\delta \mathbf{u}^*}, \mathbf{v} \right\rangle_{\Omega_t} + \frac{\epsilon^2}{2} \langle \mathbf{v}, \mathbf{H}\mathbf{v} \rangle_{\Omega_t} + O(\epsilon^3) = \frac{\epsilon^2}{2} \langle \mathbf{v}, \mathbf{H}\mathbf{v} \rangle_{\Omega_t} + O(\epsilon^3), \quad (\text{E } 2)$$

where the fact that \mathbf{u}^* is a minimum means that $\mathcal{R}[\mathbf{u}^*] = \|\delta \mathcal{R}/\delta \mathbf{u}^*\| = 0$. We then have a local quadratic model for the variation of \mathcal{R} that is governed by the Hessian operator \mathbf{H} . The second-order variation of the global residual is given by $\mathcal{R}[\mathbf{u}^* + \epsilon \mathbf{v}] = \|\delta \mathbf{r}\|_{\Omega_t}^2/2$. Linearising the local residual in (E 1) and substituting this into the previous expressions gives

$$\langle \mathbf{v}, \mathbf{H}\mathbf{v} \rangle_{\Omega_t} = \left\| \frac{\partial \mathbf{v}}{\partial t} - \mathbb{P}\mathcal{L}_{\mathbf{u}^*}\mathbf{v} \right\|_{\Omega_t}^2. \quad (\text{E } 3)$$

REFERENCES

- AHMED, M ARSLAN & SHARMA, ATI S 2020 Basis for finding exact coherent states. *Physical Review E* **101**, 12213.
- AIZAWA, YOJI 1982 Global aspects of the dissipative dynamical systems. i: — statistical identification and fractal properties of the lorenz chaos —. *Progress of Theoretical Physics* **68**, 64–84.
- ARTUSO, R., AURELL, E. & CVITANOVIC, P. 1990 Recycling of strange sets: I. cycle expansions. *Nonlinearity* **3**, 325–359.
- ASHTARI, OMID & SCHNEIDER, TOBIAS M 2023 Identifying invariant solutions of wall-bounded three-dimensional shear flows using robust adjoint-based variational techniques. *Journal of Fluid Mechanics* **977**, A7.
- AUERBACH, D., CVITANOVIC, P., ECKMANN, J. P., GUNARATNE, G. & PROCACCIA, I. 1987 Exploring chaotic motion through periodic orbits. *Phys. Rev. Lett.* **58**, 2387–2389.

- AZIMI, S., ASHTARI, O. & SCHNEIDER, T. M. 2022 Constructing periodic orbits of high-dimensional chaotic systems by an adjoint-based variational method. *Phys. Rev. E* **105**, 14217.
- BARTHEL, B., ZHU, X. & McKEON, B. J. 2021 Closing the loop: nonlinear taylor vortex flow through the lens of resolvent analysis. *Journal of Fluid Mechanics* **924**, A9.
- BENEDDINE, S., YEGAVIAN, R., SIPP, D. & LECLAIRE, B. 2017 Unsteady flow dynamics reconstruction from mean flow and point sensors: An experimental study. *Journal of Fluid Mechanics* **824**, 174–201.
- BRANDT, L., SIPP, D., PRALITS, J. O. & MARQUET, O. 2011 Effect of base-flow variation in noise amplifiers: the flat-plate boundary layer. *Journal of Fluid Mechanics* **687**, 503–528.
- BURTON, T. 2025 Resolvent-based models for nonlinear solutions of wall-bounded flows and statistical estimation of chaotic systems. PhD thesis, University of Southampton.
- BURTON, T., SYMON, S., SHARMA, A. S. & LASAGNA, D. 2025 Resolvent-based optimization for approximating the statistics of a chaotic lorenz system. *Physical Review E* **111**, 25104.
- CANUTO, C., HUSSAINI, M. Y., QUARTERONI, A. & ZANG, T. A. 1988 *Spectral Methods in Fluid Dynamics*. Springer Berlin Heidelberg.
- CHANDLER, G. J. & KERSWELL, R. R. 2013 Invariant recurrent solutions embedded in a turbulent two-dimensional kolmogorov flow. *Journal of Fluid Mechanics* **722**, 554–595.
- CHANDRASEKHAR, SUBRAHMANYAN 1961 *Hydrodynamic and Hydromagnetic Stability*. Oxford University Press.
- CHRISTIANSEN, F., CVITANOVIC, P. & PUTKARADZE, V. 1997 Spatiotemporal chaos in terms of unstable recurrent patterns. *Nonlinearity* **10**, 55–70.
- CROWLEY, CHRISTOPHER J, PUGHE-SANFORD, JOSHUA L, TOLER, WESLEY, KRYGIER, MICHAEL C, GRIGORIEV, ROMAN O & SCHATZ, MICHAEL F 2022 Turbulence tracks recurrent solutions. *Proceedings of the National Academy of Sciences* **119**, e2120665119, doi: 10.1073/pnas.2120665119.
- CVITANOVIĆ, P. 1988 Invariant measurement of strange sets in terms of cycles. *Physical Review Letters* **61**, 2729–2732.
- CVITANOVIĆ, P. 1995 Dynamical averaging in terms of periodic orbits. *Physica D: Nonlinear Phenomena* **83**, 109–123.
- CVITANOVIĆ, P. & GIBSON, J. F. 2010 Geometry of the turbulence in wall-bounded shear flows: periodic orbits. *Physica Scripta* **T142**, 014007.
- DAHLQUIST, G. & BJÖRCK, Å. 2008 *Numerical Methods in Scientific Computing, Volume I*. Society for Industrial and Applied Mathematics.
- DAVIAUD, F., HEGSETH, J. & BERGÉ, P. 1992 Subcritical transition to turbulence in plane couette flow. *Physical Review Letters* .
- DENNIS, J. E. & SCHNABEL, B. 1983 Numerical methods for unconstrained optimization and nonlinear equations. In *Prentice Hall series in computational mathematics*.
- ECKHARDT, B., DOERING, C. R. & WHITEHEAD, J. P. 2020 Exact relations between rayleigh–bénard and rotating plane couette flow in two dimensions. *Journal of Fluid Mechanics* **903**, R4.
- ECKHARDT, BRUNO, GROSSMANN, SIEGFRIED & LOHSE, DETLEF 2007 Torque scaling in turbulent taylor–couette flow between independently rotating cylinders. *Journal of Fluid Mechanics* **581**, 221–250.
- FAISST, H. & ECKHARDT, B. 2003 Traveling waves in pipe flow. *Phys. Rev. Lett.* **91**, 224502.
- FARAZMAND, M. 2016 An adjoint-based approach for finding invariant solutions of navier–stokes equations. *Journal of Fluid Mechanics* **795**, 278–312.
- FAZENDEIRO, L., BOGHOSIAN, B. M., COVENEY, P. V. & LÄTT, J. 2010 Unstable periodic orbits in weak turbulence. *Journal of Computational Science* **1**, 13–23.
- FRIGO, MATTEO & JOHNSON, STEVEN G. 2005 The design and implementation of fftw3. *Proceedings of the IEEE* **93**, 216–231.
- GARNAUD, X., LESSHAFFT, L., SCHMID, P. J. & HUERRE, P. 2013 The preferred mode of incompressible jets: linear frequency response analysis. *Journal of Fluid Mechanics* **716**, 189–202.
- GAYME, D. 2010 A robust control approach to understanding nonlinear mechanisms in shear flow turbulence. PhD thesis, California Institute of Technology.
- GAYME, D. F. & MINNICK, B. A. 2019 Coherent structure-based approach to modeling wall turbulence. *Phys. Rev. Fluids* **4**, 110505.
- GIBSON, J. F., HALCROW, J. & CVITANOVIC, P. 2008 Visualizing the geometry of state space in plane couette flow. *Journal of Fluid Mechanics* **611**, 107–130.
- GÓMEZ, F., BLACKBURN, H. M., RUDMAN, M., SHARMA, A. S. & McKEON, B. J. 2016 A reduced-order

- model of three-dimensional unsteady flow in a cavity based on the resolvent operator. *Journal of Fluid Mechanics* **798**, R2.
- HAGER, W. W. & ZHANG, H. 2005 A new conjugate gradient method with guaranteed descent and an efficient line search. *SIAM Journal on Optimization* **16**, 170–192.
- HIWATASHI, KAZUAKI, ALFREDSSON, P H, TILLMARK, NILS & NAGATA, M 2007 Experimental observations of instabilities in rotating plane couette flow. *Physics of Fluids* **19**, 048103.
- HOPF, E. 1942 Abzweigung einer periodischen lösung von einer stationären lösung eines differentialsystems. *Ber. Verh. Sächs. Akad. Wiss. Leipzig Math.-Nat. Kl.* **94**, 1–22.
- HOPF, E. 1948 A mathematical example displaying features of turbulence. *Communications on Pure and Applied Mathematics* **1**, 303–322.
- ITANO, T. & GENERALIS, S. C. 2009 Hairpin vortex solution in planar couette flow: A tapestry of knotted vortices. *Physical Review Letters* **102**, 114501.
- JIN, BO, ILLINGWORTH, SIMON J & SANDBERG, RICHARD D 2022 Resolvent-based approach for $\{H_2\}$ -optimal estimation and control: an application to the cylinder flow. *Theoretical and Computational Fluid Dynamics* **36**, 491–515.
- KAWAHARA, G. & KIDA, S. 2001 Periodic motion embedded in plane couette turbulence: regeneration cycle and burst. *Journal of Fluid Mechanics* **449**, 291–300.
- KAWAHARA, GENTA, UHLMANN, MARKUS & VAN VEEN, LENNAERT 2012 The significance of simple invariant solutions in turbulent flows. *Annual Review of Fluid Mechanics* **44**, 203–225.
- KLEISER, L. & SCHUMANN, U. 1980 *Treatment of Incompressibility and Boundary Conditions in 3-D Numerical Spectral Simulations of Plane Channel Flows*, pp. 165–173. Vieweg+Teubner Verlag.
- KRYGIER, MICHAEL C, PUGHE-SANFORD, JOSHUA L & GRIGORIEV, ROMAN O 2021 Exact coherent structures and shadowing in turbulent taylor–couette flow. *Journal of Fluid Mechanics* **923**, A7.
- LAKOBA, T I & YANG, J 2007 A mode elimination technique to improve convergence of iteration methods for finding solitary waves. *Journal of Computational Physics* .
- LAN, Y. & CVITANOVIĆ, P. 2004 Variational method for finding periodic orbits in a general flow. *Physical Review E - Statistical Physics, Plasmas, Fluids, and Related Interdisciplinary Topics* **69**, 10.
- LASAGNA, D., TUTTY, O. R. & CHERNYSHENKO, S. 2016 Flow regimes in a simplified taylor–couette-type flow model. *European Journal of Mechanics - B/Fluids* **57**, 176–191.
- LEZIUS, DIETRICH K & JOHNSTON, JAMES P 1976 Roll-cell instabilities in rotating laminar and trubulent channel flows. *Journal of Fluid Mechanics* **77**, 153–174.
- LI, X. & LASAGNA, D. 2025 Space-time nonlinear reduced-order modelling for unsteady flows. *arXiv* .
- MCKEON, B. J. & SHARMA, A. S. 2010 A critical-layer framework for turbulent pipe flow. *Journal of Fluid Mechanics* **658**, 336–382.
- MOGENSEN, PATRICK KOFOD & RISETH, ASBJØRN NILSEN 2018 Optim: A mathematical optimization package for julia. *Journal of Open Source Software* **3**, 615.
- MONS, V. & MARQUET, O. 2021 Linear and nonlinear sensor placement strategies for mean-flow reconstruction via data assimilation. *Journal of Fluid Mechanics* **923**, A1.
- NAGATA, M. 1990 Three-dimensional finite-amplitude solutions in plane couette flow: bifurcation from infinity. *Journal of Fluid Mechanics* **217**, 519–527.
- NAGATA, M 1997 Three-dimensional traveling-wave solutions in plane couette flow. *Physical Review E* **55**, 2023–2025.
- NAGATA, M. 2013 A note on the mirror-symmetric coherent structure in plane couette flow. *Journal of Fluid Mechanics* **727**, R1.
- NAGATA, M., SONG, B. & WALL, D. P. 2021 Onset of vortex structures in rotating plane couette flow. *Journal of Fluid Mechanics* **918**, A2.
- NOCEDAL, J. & WRIGHT, S. 2006 *Numerical Optimization*, 2nd edn. Springer-Verlag New York.
- OKINO, S., NAGATA, M., WEDIN, H. & BOTTARO, A. 2010 A new nonlinear vortex state in square-duct flow. *Journal of Fluid Mechanics* **657**, 413–429.
- PAGE, JACOB, NORGAARD, PETER, BRENNER, MICHAEL P & KERSWELL, RICH R 2024 Recurrent flow patterns as a basis for two-dimensional turbulence: Predicting statistics from structures. *Proceedings of the National Academy of Sciences* **121**, e2320007121.
- PRINGLE, C. C. T. & KERSWELL, R. R. 2007 Asymmetric, helical, and mirror-symmetric traveling waves in pipe flow. *Physical Review Letters* **99**, 74502.
- RUELLE, D. & TAKENS, F. 1971 On the nature of turbulence. *Communications in Mathematical Physics* **20**, 167–192.

- SAAD, YUCEF & SCHULTZ, MARTIN H 1986 Gmres: A generalized minimal residual algorithm for solving nonsymmetric linear systems. *SIAM Journal on Scientific and Statistical Computing* **7**, 856–869.
- SHARMA, A. S. 2019 Elements of resolvent methods in fluid mechanics: notes for an introductory short course v0.3. *arXiv* pp. 1–24.
- SHARMA, ATI S, MOARREF, RASHAD, McKEON, BEVERLEY J, PARK, JAE SUNG, GRAHAM, MICHAEL D & WILLIS, ASHLEY P 2016 Low-dimensional representations of exact coherent states of the navier-stokes equations from the resolvent model of wall turbulence. *Physical Review E* **93**, 21102.
- SURI, BALACHANDRA, KAGEORGE, LOGAN, GRIGORIEV, ROMAN O & SCHATZ, MICHAEL F 2020 Capturing turbulent dynamics and statistics in experiments with unstable periodic orbits. *Physical Review Letters* **125**, 64501.
- SYMON, S., ROSENBERG, K., DAWSON, S. T. M. & McKEON, B. J. 2018 Non-normality and classification of amplification mechanisms in stability and resolvent analysis. *Physical Review Fluids* **3**.
- SÁNCHEZ, J., NET, M., GARCÍA-ARCHILLA, B. & SIMÓ, C. 2004 Newton–krylov continuation of periodic orbits for navier–stokes flows. *Journal of Computational Physics* **201**, 13–33.
- TEMAM, R. 1984 *Navier-Stokes equations : theory and numerical analysis*. AMS Chelsea Pub.
- TOMOAKI, I. & SADAYOSHI, T. 2001 The dynamics of bursting process in wall turbulence. *Journal of the Physical Society of Japan* **70**, 703–716.
- TSUKAHARA, T., TILLMARK, N. & ALFREDSSON, P. H. 2010 Flow regimes in a plane couette flow with system rotation. *Journal of Fluid Mechanics* **648**, 5–33.
- UHLMANN, M., KAWAHARA, G. & PINELLI, A. 2010 Traveling-waves consistent with turbulence-driven secondary flow in a square duct. *Physics of Fluids* **22**, 084102.
- VAN VEEN, L., KIDA, S. & KAWAHARA, G. 2006 Periodic motion representing isotropic turbulence. *Fluid Dynamics Research* **38**, 19–46.
- VEEN, L. VAN, VELA-MARTÍN, A. & KAWAHARA, G. 2019 Time-periodic inertial range dynamics. *Physical Review Letters* **123**, 134502.
- VISWANATH, D. 2007 Recurrent motions within plane couette turbulence. *Journal of Fluid Mechanics* **580**, 339–358.
- VISWANATH, D. 2009 The critical layer in pipe flow at high reynolds number. *Philosophical Transactions of the Royal Society A: Mathematical, Physical and Engineering Sciences* **367**, 561–576.
- WALEFFE, F. 1998 Three-dimensional coherent states in plane shear flows. *Phys. Rev. Lett.* **81**, 4140–4143.
- WALEFFE, F. 2001 Exact coherent structures in channel flow. *Journal of Fluid Mechanics* **435**, 93–102.
- WALEFFE, FABIAN 2009 Exact coherent structures in turbulent shear flows. In *Turbulence and Interactions* (ed. Michel Deville, Thien-Hiep Lê & Pierre Sagaut), pp. 139–158. Springer Berlin Heidelberg.
- WANG, B., AYATS, R., DEGUCHI, K., MESEGUER, A. & MELLIBOVSKY, F. 2025 Mathematically established chaos and forecast of statistics with recurrent patterns in taylor–couette flow. *Journal of Fluid Mechanics* **1011**, R2.
- WEDIN, H., BOTTARO, A. & NAGATA, M. 2009 Three-dimensional traveling waves in a square duct. *Physical Review E* **79**, 65305.
- WEDIN, H. & KERSWELL, R. R. 2004 Exact coherent structures in pipe flow: travelling wave solutions. *Journal of Fluid Mechanics* **508**, 333–371.
- WILLIS, A P, CVITANOVIĆ, P & AVILA, M 2013 Revealing the state space of turbulent pipe flow by symmetry reduction. *Journal of Fluid Mechanics* **721**, 514–540.
- YALNIZ, G., HOF, B. & BUDANUR, N. B. 2021 Coarse graining the state space of a turbulent flow using periodic orbits. *Physical Review Letters* **126**, 244502.
- YANG, J. & LAKOBA, T. I. 2007 Universally-convergent squared-operator iteration methods for solitary waves in general nonlinear wave equations. *Studies in Applied Mathematics* **118**, 153–197.
- YIH, CHIA-SHUN 1965 *Dynamics of Nonhomogeneous Fluids*. Macmillan.